DESIGN AND NAVIER-STOKES ANALYSIS OF HYPERSONIC WIND TUNNEL NOZZLES

by

James R. Benton

A thesis submitted to the Graduate Faculty of
North Carolina State University
in partial fulfillment of the
requirements for the Degree of
Master of Science

Department of Mechanical and Aerospace Engineering

Raleigh

1 9 8 9

Approved By:

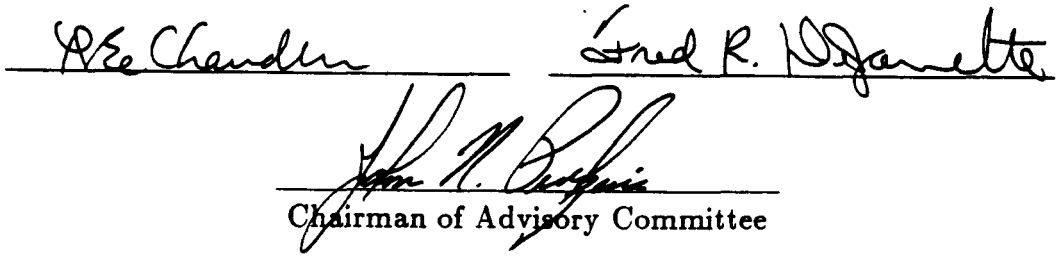

Chairman of Advisory Committee

Abstract

Benton, James R. Design and Navier-Stokes Analysis of Hypersonic Wind Tunnel Nozzles. (Under the direction of Dr. John N. Perkins)

Four hypersonic wind tunnel nozzles ranging in Mach number from 6 to 17 are designed with the method of characteristics and boundary layer approach (MOC/BL) and analyzed with a Navier-Stokes solver. Limitations of the MOC/BL approach when applied to thick high speed boundary layers with non-zero normal pressure gradients are investigated. Working gases include ideal air, thermally perfect nitrogen and virial CF_4. Agreement between the design conditions and Navier-Stokes solutions for ideal air at Mach 6 is good. Thermally perfect nitrogen showed poor agreement at Mach 13.5 and Mach 17. Navier-Stokes solutions for CF_4 are not obtained, but comparison of the effects of low γ to those of high Mach number suggests that the Navier-Stokes solution would not compare well with design.

Acknowledgements

The author would like to thank Dr. John N. Perkins for the opportunity to work with him on this project, for serving as Graduate Committee Chairman and for making the necessary contractual arangements for this research effort. His willingness to work together and provide valuable guidance is gratefully acknowledged. Thanks are also extended to Dr. H. A. Hassan and Dr. D. S. McRae of NCSU for many helpful discussions. The progress of this research is indebted to Dr. E. C. Anderson and Dr. A. Kumar of NASA Langley Research Center for discussions and guidance in the use of their computer programs.

The author would also like to thank the Mechanical and Aerospace Engineering Department of NCSU and the Hypersonic Aerodynamics Experimental Branch of NASA Langley Research Center for the use of their facilities and the financial support that helped make this thesis possible. The research for this thesis was supported in part by NASA Grant NCC1-109.

Table of Contents

Nomenclature

a	speed of sound
A	cross sectional area
A^*	cross sectional area of nozzle throat
A_i, B_i, C_i, k	constants in CF_4 eqn. of state, eqs. 4.2-4.4
$\hat{b}$	volume of gas molecules
C	Levy-Lees variables, eq B.7
C_p	constant pressure specific heat
C_v	constant volume specific heat
C_+	left running characteristic wave
C_-	right running characteristic wave
dt	time step
e	internal energy per unit mass
E	total energy per unit mass
fdt	Courant-Fredriechs-Lewy number
F	Levy-Lees variable, eq. B.6
g	Levy-Lees variable, eq. B.8
h	enthalpy
H	source term, eq. 2.1
H_o	reservoir enthalpy
J	Jacobian of the numerical transformation
k, k_l	coefficient of thermal conductivity
L_c	characteristic length for nondimensionalization
$\dot{m}$	massflow rate
M	Mach number; flux vector, eq 2.1
N	flux vector, eq. 2.1
P	pressure
P_o	reservoir pressure; total pressure
Pr	Prandtl number
Pr_t	turbulent Prandtl number, 0.9
q_j	heat transfer in the j-direction
r	radial spacial coordinate
r_{cr}	radial location at Mach 1
R	gas constant
Re	Reynolds number
$\overline{R}$	universal gas constant
s	curvilinear coordinate, eq. A.13

S	entropy
t	time
T	temperature
T_c	characteristic temperature for nondimensionalization
T_o	reservoir temperature; total temperature
u	axial velocity component
U	vector of conservation variables, eq. 2.1
v	radial velocity component
$\overline{v}$	molar specific volume
V	velocity magnitude; Levy-Lees variable, eq. B.6
V_c	characteristic velocity for nondimensionalization
W	radial flow velocity, eq A.11
x	axial spacial coordinate
y	radial spacial coordinate
y_{corr}	corrected wall coordinate
y_{inv}	inviscid wall coordinate
β	Levy-Lees variable, eq. B.7
γ	ratio of specific heats
δ	boundary layer thickness
$\delta_{i,j}$	Kronecker delta, eq. C.2
δ^*	displacement thickness
ε^+	eddy viscosity
η	coordinate in transformed plane; Levy-Lees coordinate, eq. B.5
θ	flow angle to horizontal, eq. A.3
θ_c, θ_{max}	maximum turning angle
θ_I	Prandtl-Meyer expansion function, eq. A.6
μ	molecular coefficient of viscosity, Mach angle, eq A.5
μ_c	characteristic viscosity coefficient for nondimensionalization
μ_l	laminar viscosity coefficient
μ_t	eddy viscosity
$\mathcal{V}$	specific volume
ξ	coordinate in transformed plane; Levy-Lees coordinate, eq. B.4
ρ	density
ρ_e	characteristic density for nondimensionalization
ρ_t	total density
$\rho C_p \overline{u_i' T'}$	turbulent heat transfer, eq. C.1
$\overline{\rho u_i' u_j'}$	Reynolds stress, eq. C.2
$\sigma_{i,j}$	stress tensor
$\tau_{i,j}$	stress tensor
ψ	stream function, eq. A.11
ψ_{lim}	stream function at displaced wall
ω	vorticity

subscripts

c	characteristic variable
cr	Mach 1 in source flow
e	boundary layer edge value
i	differentiation w.r.t. i-direction
l	laminar
min	minimum
max	maximum
NS	Navier-Stokes
r	reference value
t	differentiation w.r.t. time
w	wall value
∞	freestream value

1 Introduction

The recently renewed interest in hypersonic research, due to such projects as the National Aero-Space Plane (NASP) and the Aero-assisted Orbital Transfer Vehicle (AOTV), has reemphasized the need for state-of-the-art test facilities in the hypersonic flight regime. However, a steady decline in funding in this area over the past 25 years has left the ground testing community unprepared for the challenge. Since the early 1970's, the number of active hypersonic wind tunnels has dropped from 70 to about 15. Only one major hypersonic wind tunnel has been developed during this period and many of the remaining facilities are in need of upgrades [1]. Of prime importance in any aerodynamic wind tunnel operation is high quality flow. That is, flow in the tunnel test section which is highly uniform with regards to Mach number, total pressure and flow angularity in the radial, axial and transverse directions. The necessity for uniform flow in ground testing facilities is well understood, but as methods of Computational Fluid Dynamics (CFD) continue to mature, the benefits of flow uniformity to CFD grow clearer. Navier-Stokes and Euler codes developed for supersonic and hypersonic flow analysis generally hold upstream boundaries constant at some uniform freestream condition. So, the ability to deliver uniform flow grants the hypersonic wind tunnel the additional objective of validating computer solutions. In turn, each time computational data is confirmed by experiment, confidence in CFD is elevated and the ability to provide advanced designs is enhanced.

The formidable task of providing high quality flow in a wind tunnel operation is achieved almost exclusively through nozzle design and construction. Presently, of the seven operational hypersonic wind tunnels at NASA Langley's Hypersonic Facilities Complex (HFC), three have unacceptable flow characteristic in the test section — the Hypersonic Nitrogen Tunnel, the Hypersonic Helium Tunnel, and the Hypersonic CF_4 Tunnel. The importance of these tunnels to the maintenance of a continuous and well-rounded testing facility at HFC prompted NASA to propose upgrades to these and other wind tunnels. Improved flow quality through nozzle redesign for three HFC wind tunnels has received highest priority in these upgrades.

In addition to redesigning these nozzles, two new nozzles are proposed for manufacture. The first is a Mach 6 air nozzle for an undeveloped wind tunnel which is to be re-machined out of an existing nozzle that was originally designed for Mach 10. The second is another nozzle for the Hypersonic Nitrogen Tunnel designed for Mach 13.5. Design conditions and constraints for all the proposed nozzles are presented in Table 1.

The Hypersonic Nitrogen Tunnel is an axisymmetric blowdown tunnel with an open-jet test section. The nozzle is 10.5 feet long with a 16 inch diameter exit designed for Mach 17 flow. The results of a tunnel calibration, Fig. 1.1, show a severe disturbance in the test section [2]. Irregularities are evident up to two inches across the centerline, which, in conjunction with the tunnel's inherently thick boundary layer, limits the size of models to about $1\frac{1}{2}$ to 2 inches in total thickness [3].

At the test section of the CF_4 tunnel, a centerline disturbance appears as a Mach number spike corresponding roughly to a 13 percent rise in pitot pressure [3]. The pitot rake profile of the test section is plotted in Fig. 1.2 and shows uniform flow across the axisymmetric nozzle with the exception of the centerline [5]. Thompson and Sutton [6] discovered a discrepancy existing between the reference enthalpy of the Method of Characteristics and boundary layer codes used in the nozzle's design by Johnson et al. [7]. This inconsistency produced errors in the density profile of the boundary layer which, in turn, gave an erroneous displacement thickness calculation. The centerline disturbance, which is the result of the error in displacement thickness, severely limits the physical size of models tested in the facility since any model must be situated between the centerline disturbance and the wall boundary layer. For the 20 inch diameter nozzle with roughly 1.5 inches of boundary layer at design conditions the model size is decreased from 18.5 inches thick to less than 9.25 inches thick in the presence of the centerline disturbance.

All nozzles were designed using the classical approach of iteration between a Method of Characteristics (MOC) code and a state-of-the-art boundary layer code until all design constraints were met. This iterative design approach will be referred to as MOC/BL. The theory used for the MOC design procedure is based on the method published by C. B. Johnson et al. [8] , the details of which are left to Appendix A. Figure 1.3 is a schematic of the inviscid portion of a supersonic nozzle that shows the various flow regions. The line DE represents the final char-

acteristic along which the Mach number equals the design Mach number and the flow angularity is zero. The region BCD is known as the radial flow region and the centerline Mach number here is calculated using radial flow equations in the design phase. With the MOC approach, one must specify both the distribution of Mach number or velocity on the centerline between points A and B and the maximum turning angle at the inflection point C. These parameters effect both the shape and length of the expansion region [6]. Boundary Layers were generated with a robust, state-of-the-art code developed by E. C. Anderson [9]. Some details concerning the boundary layer code used here are presented in Appendix B.

MOC analysis of the CF_4 and Mach 17 nitrogen characteristic contours were performed during the course of this research, but are not included in this thesis. For both cases, the MOC analysis procedure agreed with the design. Also, analysis of the existing CF_4 nozzle at off design conditions was performed and agreement with experiment was qualitatively good. Further confidence in the MOC/BL procedures was obtained by Thompson and Sutton's [6] prediction of the Mach number spike present in the original CF_4 tunnel by an MOC analysis approach. Also, an independent Euler analysis of the Mach 17 N_2 characteristic contour gave uniform Mach 17.2 flow when it was started with a supersonic inflow profile generated by the MOC design code.

Confirmation of the designs by an MOC analysis procedure, however, proves only self-consistency between the two MOC/BL design and analysis procedures and not

absolute confidence in the designs. And even with certain independent validations such as off-design conditions and Euler solutions, there still remains some question as to the applicability of the MOC/BL procedures to hypersonic nozzle design with its thick, highly turbulent, supersonic boundary layers. The philosophy behind MOC/BL as applied to viscous flow centers around the idea of the displacement thickness, δ^*. Figure 1.4 schematically illustrates the idea behind δ^*. In words, it is the distance that the actual wall boundary would have to be displaced such that the mass flow in a uniform *inviscid* boundary layer profile, moving at the edge velocity, U_e, is just equal to the mass flow in the original viscous profile. At this new displaced wall, the characteristic waves are assumed to reflect or cancel, depending upon the local slope of the new inviscid wall.

$$\delta^* = \int_o^{y_e} \left(1 - \frac{\rho u}{\rho_e U_e}\right)(r_o - y\cos\theta)\,dy - \frac{\Delta w_o}{\rho_e u_e} \tag{1.1}$$

It is calculated by trapezoidal integration of eq. (1.1) in the boundary layer starting at the wall until the integrand is close to zero at the boundary layer edge. This technique works well for thin boundary layers because the displacement thickness—where inviscid characteristic waves are assumed to be reflected—and where the characteristic is actually reflected within the viscous boundary layer, are more likely to be near the same location. As the boundary layer grows thicker, or as the edge Mach number increases, more supersonic flow is found inside the boundary layer and perhaps even inside δ^*. In the supersonic boundary layer the characteristics would tend to curve towards the wall as the Mach number decreased and could therefore reflect

from the wall in a different axial and radial location than the δ^* approach predicts. An error such as this would undermine the relationship between the physics of the flow and the mathematical model. For similar reasons the viscous/inviscid approach is more accurate for laminar boundary profiles than for turbulent ones since turbulent boundary layers generally have steeper velocity profiles where the flow could remain supersonic very close to the wall. For hypersonic flow, MOC predicts that a long, slow turning contour is necessary for the proper cancellation of characteristic waves to produce uniform flow at the nozzle exit. Because of the extended length of these nozzles, the boundary layer growth is significant. Another question arises here as to the validity of using MOC and boundary layer approach. Specifically, as the viscous interaction parameter increases as it does in hypersonic flow and as the boundary layer thickness increases, then the assumption of zero normal pressure gradient used in the boundary layer equations becomes less viable. For the present designs, the boundary layers are thick, turbulent and contain a large proportion of supersonic flow. They are also characterized by exit Mach numbers between 6 and 17. Therefore, a Navier-Stokes analysis of the nozzles is desired as an independent confirmation of the designs.

Design and Navier-Stokes analysis results of four of the proposed 5 wind tunnel nozzles are discussed in this thesis. These nozzles are designed to deliver uniform flow of ideal air at Mach 6 (Air) , thermally perfect N_2 at Mach 13.5 ($N_2 - 13$) and Mach 17 ($N_2 - 17$) and virial CF_4 at Mach 6 (CF_4). The objective for this research is

twofold. Obviously, high quality designs are desired to upgrade HFC test facilities. But inherent in this effort is the second objective to survey and evaluate current design capabilities as applied to high Mach number contoured nozzles.

The Navier-Stokes solver, developed by Adjay Kumar [11], was obtained from LRC and the appropriate changes were made to accommodate the three gases. Although the thermodynamic character of the present working gases vary extensively, one Navier-Stokes solver was developed that can run these and virtually any single specie gas with a bare minimum of changes between cases. This code utilizes tabular data to replace the respective equation of state throughout. The exact same thermodynamics that are used in the MOC procedures are used in the Navier-Stokes solver in this approach, therefore eliminating errors due to inconsistent thermodynamics. The approach does, however, require the development of a separate computer program or driver for each gas to establish the required tabular equation of state. This approach is necessary when analyzing the CF_4 nozzle because of its non-standard equation of state. CF_4 has a virial equation of state and can be solved explicitly only for pressure. To back out other state variables would certainly require an iterative procedure or, as in this procedure, table look-up.

2 Governing Equations

The axisymmetric Navier-Stokes equations (2.1), are used to describe the flow-field. These equations are parabolic in time and elliptic in space and are written here in weak conservation form.

$$U_t + M_x + \frac{1}{y}(yN)_y + \frac{H}{y} = 0 \tag{2.1}$$

where

$$U = \begin{bmatrix} \rho \\ \rho u \\ \rho v \\ \rho E \end{bmatrix}$$

$$M = \begin{bmatrix} \rho u \\ \rho u^2 + \sigma_{xx} \\ \rho uv + \tau_{xy} \\ (\rho E + \sigma_{xx})u + \tau_{xy}v + q_x \end{bmatrix}$$

$$N = \begin{bmatrix} \rho v \\ \rho uv + \tau_{xy} \\ \rho v^2 + \sigma_{yy} \\ (\rho E + \sigma_{yy})v + \tau_{xy}u + q_y \end{bmatrix}$$

$$H = \begin{bmatrix} 0 \\ 0 \\ -\sigma_{\theta\theta} \\ 0 \end{bmatrix}$$

and

$$\begin{aligned}
E &= e + \tfrac{1}{2}(u^2 + v^2) \\
\sigma_{xx} &= p + \tfrac{2}{3}\tfrac{\mu}{Re}\left(\tfrac{\partial v}{\partial y} - 2\tfrac{\partial u}{\partial x} + \tfrac{v}{y}\right) \\
\sigma_{yy} &= p + \tfrac{2}{3}\tfrac{\mu}{Re}\left(\tfrac{\partial u}{\partial x} - 2\tfrac{\partial v}{\partial y} + \tfrac{v}{y}\right) \\
\sigma_{\theta\theta} &= p + \tfrac{2}{3}\tfrac{\mu}{Re}\left(\tfrac{\partial u}{\partial x} + \tfrac{\partial v}{\partial y} - 2\tfrac{v}{y}\right) \\
\tau_{xy} &= -\tfrac{\mu}{Re}\left(\tfrac{\partial u}{\partial y} + \tfrac{\partial v}{\partial x}\right) \\
q_x &= -\left(\tfrac{\mu_l}{Pr} + \tfrac{\mu_t}{Pr_t}\right)\tfrac{C_p}{Re}\tfrac{\partial T}{\partial x} \\
q_y &= -\left(\tfrac{\mu_l}{Pr} + \tfrac{\mu_t}{Pr_t}\right)\tfrac{C_p}{Re}\tfrac{\partial T}{\partial y} \\
\mu &= \mu_l + \mu_t \\
Pr &= \frac{C_p \mu_l}{k_l}
\end{aligned}$$

For the ideal gas and CF_4 case, the above equations are written in terms of the following non-dimensional variables. For the thermally perfect N_2 cases, dimensional

forms of the above equations are used.

$$x = \tilde{x}/L_c \quad y = \tilde{y}/L_c$$

$$t = \tilde{t}V_c/L_c \quad p = \tilde{p}/\rho_c V_c^2$$

$$\rho = \tilde{\rho}/\rho_c \quad T = \tilde{T}/T_c$$

$$u = \tilde{u}/V_c \quad v = \tilde{v}/V_c$$

$$h = \tilde{h}/V_c^2 \quad \mu = \tilde{\mu}/\mu_c$$

$$Re = \frac{\rho_c V_c L_c}{\mu_c}$$

where the $\sim$ values are dimensional and dimensional constants are defined as,

L_c = nozzle throat radius

V_c = stagnation speed-of-sound

ρ_c = stagnation density

T_c = stagnation temperature

μ_c = stagnation viscosity

To complete the set of governing equations, appropriate gas models are needed for each type gas — ideal, thermally perfect, real-gas (see Chapter 4) — as well as relations for the transport properties, μ_l and Pr. For ideal gases, μ_l is calculated using Sutherland's viscosity law and Pr is held constant. For thermall perfect and virial gases, the laminar transport properties are interplolated from precalculated tables.

Appendix C illustrates the procedure for determining the turbulent transport properties, Pr_t and μ_t.

The original Navier-Stokes solver was developed for two dimensions [11] and the equations were integrated in strong conservation law form (2.2).

$$U_t + M_x + N_y = 0 \tag{2.2}$$

An axisymmetric patch was later ammended to the code and the governing equations are now in weak conservation law form (2.3) Equation (2.3) is obtained by a simple application of the chain rule to the third term of equation (2.1).

$$U_t + M_x + N_y + \frac{N + H}{y} = 0 \tag{2.3}$$

3 Integration Technique

The nozzle flow domain is discretized with a grid similar to Figure 3.0a. An algebraic numerical transformation provides direct grid control through a stretching parameter [11]. Grid points are compressed near the wall to resolve the boundary layer and near the centerline to capture the mathematical discontinuity. Governing equations are transformed to a uniformly spaced grid and integrated using MacCormmack's explicit *predictor-corrector* scheme. This scheme is second order accurate in time and space and straightforward to program. In the transformed plane, (ξ, η), the governing equations become,

$$\frac{U_t}{J} + (My_\eta - Nx_\eta)_\xi + (Nx_\xi - My_\xi)_\eta + \frac{N+H}{yJ} = 0 \tag{3.1}$$

where the Jacobian of the transformation, J is defined,

$$J = 1/(x_\xi y_\eta - x_\eta y_\xi)$$

The unsteady equations (eq. (3.1)) are stepped through time using the two step procedure, eqs (3.2) and (3.3), and viscous time step, eqn (3.3), until a steady flow condition is achieved and the solution is converged.

$$\overline{U^{n+1}} = U^n - dt\left[(My_\eta - Nx_\eta)^n + (Nx_\xi - My_\xi)^n + H^n\right] \tag{3.2}$$

$$\begin{aligned} U^{n+1} &= \frac{1}{2}\left\{\left(U^n + \overline{U^{n+1}}\right)\right. \\ &\quad \left. -dt\left[(My_\eta - Nx_\eta)^{\overline{n+1}} + (Nx_\xi - My_\xi)^{\overline{n+1}} + H^{\overline{n+1}}\right]\right\} \end{aligned}$$

$$dt = \left(\frac{y_\eta \mathrm{fdt}}{a + |v|} \right)_{min} \tag{3.3}$$

The convective terms or outer derivatives (the second and third terms of equation (3.1)) for the predictor step are evaluated with forward differences at every odd time step and with backward differences at every even time step. These terms are evaluated with opposite direction differencing for the respective corrector steps. The stress derivatives or inner derivatives (these terms are internal to M and N and are defined in equation set (4.1)) are calculated with differences of opposite direction than their respective outer derivatives. Thus, the viscous stresses and heat transfer in flux vectors for a forward predictor step will be calculated with backward differencing. This reversal of the differencing is found to improve flow symmetry at the reflective centerline [11].

4 Gas Model

Three gas models are used in the Navier-Stokes solver. The first is the simple calorically perfect gas characterized by constant C_p and C_v and adherence to the standard gas law. This model is used to analyze the Air nozzle and while experimenting with new calculations, turbulence models, grids, differencing techniques, etcetera. The second gas model is that of a thermally perfect gas. Here the gas cannot be chemically reacting and intermolecular forces are ignored, so again, it is assumed that the gas adheres to the standard gas law. The specific heats, enthalpy and internal energy depend only upon temperature.

$$e = e(T)$$

$$h = h(T)$$

$$C_p = \frac{dh}{dT}$$

$$C_v = \frac{de}{dT}$$

The third gas model is that of a virial coefficient gas. Virial gases follow an equation of state of the general form,

$$\frac{P\overline{v}}{\overline{R}T} = 1 + \frac{B(T)}{\overline{v}} + \frac{C(T)}{\overline{v}^2} + \frac{D(T)}{\overline{v}^3} + \cdots, \tag{4.1}$$

where $\overline{v}$ is the molar specific volume, $\overline{R}$ is the universal gas constant, and $B(T), C(T)$, and $D(T)$ are temperature dependant virial coefficients. These coefficients are

derived through statistical thermodynamics to account for intermolecular forces. Thus, virial gases are, by definition, real gases such that,

$$e = e(p, T)$$

$$h = h(p, T)$$

$$C_p = \left(\frac{\partial h}{\partial T}\right)_p$$

$$C_v = \left(\frac{\partial e}{\partial T}\right)_v .$$

4.1 Nitrogen Nozzles

The $N_2 - 17$ and $N_2 - 13$ are analyzed using the thermally perfect gas model. For this case, transport properties, μ_l and Pr_l, and relationships for h, e and C_p are tabulated as functions of temperature. The tables are used at every predictor and corrector step during the decomposition of the solution vector, U, using the relationship between e, the independent variable and T. The transport properties are updated every twenty iterations.

4.2 CF_4 Nozzle

The nozzle for the Hypersonic CF_4 Tunnel is analyzed using the real gas relationships. Because intermolecular forces in CF_4 gas (tetraflouromethane) remain significant throughout its vapor state, the following 13 coefficient virial equation of

state is required.

$$P = \frac{RT}{\mathcal{V}-\hat{b}} + \frac{A_2 + B_2T + C_2e^{-KT}}{(\mathcal{V}-\hat{b})^2} + \frac{A_3 + B_3T + C_3e^{-KT}}{(\mathcal{V}-\hat{b})^3} + \frac{A_4 + B_4T}{(\mathcal{V}-\hat{b})^4} + \frac{A_5 + B_5T + C_5e^{-KT}}{(\mathcal{V}-\hat{b})^5} + (A_6 + B_6T)e^{\alpha\mathcal{V}}. \quad (4.2)$$

The variable $\hat{b}$ is intended to correct for the volume occupied by the gas molecules.

CF_4 is used as a wind tunnel gas because it is heavy ($\mathcal{M} = 88.01$) and allows high Reynolds numbers (Re) to be achieved. Real gas relationships for enthalpy and entropy are given by equations (4.3) and (4.4). The reference conditions for the enthalpy and entropy equations are defined as,

$$\begin{aligned} P_r &= 6894.8\tfrac{N}{m^2} \\ T_r &= 455.6K \\ \mathcal{V}_r &= 1/\rho_r = 6.2428\tfrac{m^3}{kg} \\ h_r &= 4.6571x10^5\tfrac{J}{kg} \\ S_r &= 3542.0\tfrac{J}{kgK} \end{aligned}$$

$$
\begin{aligned}
h - h_r = {} & a_4(T - T_r) + \frac{b_4}{2}(T^2 - T_r^2) + \frac{c_4}{3}(T^3 - T_r^3) + \frac{d_4}{4}(T^4 - T_r^4) + \left[e^{-KT}(KT + 1) - e^{-KT_r}(KT_r + 1)\right] \\
& \cdot \left[\frac{C_2}{\mathcal{V}_r - b} + \frac{C_3}{2(\mathcal{V}_r - b)^2} + \frac{C_5}{4(\mathcal{V} - b)^5}\right] + \mathcal{V}_r \left[\frac{R}{\mathcal{V}_r - b}(T - T_r) + \frac{B_2(T - T_r) + c_2(e^{-KT} - e^{-KT_r})}{(\mathcal{V}_r - b)^2}\right. \\
& + \frac{B_3(T - T_r) + c_3(e^{-KT} - e^{-KT_r})}{(\mathcal{V}_r - b)^3} + \frac{B_4(T - T_r)}{(\mathcal{V} - b)^4} + \frac{B_5(T - T_r) + C_5(e^{-KT} - e^{-KT_r})}{(\mathcal{V}_r - b)^5} \\
& \left. + B_6 e^{\alpha \mathcal{V}_r}(T - T_r)\right] - \left\{RT\left[\ln\left(\frac{\mathcal{V} - b}{\mathcal{V}_r - b}\right) + \frac{b}{\mathcal{V}_r - b} - \frac{b}{\mathcal{V} - b}\right]\right. \\
& + 2(A_2 + B_2 T + C_2 e^{-KT})\left[\frac{1}{\mathcal{V}_r - b} + \frac{b}{2(\mathcal{V}_r - b)^2} - \frac{1}{\mathcal{V} - b} - \frac{b}{2(\mathcal{V} - b)^2}\right] \\
& + 3(A_3 + B_3 T + C_3 e^{-KT})\left[\frac{1}{2(\mathcal{V}_r - b)^2} + \frac{b}{3(\mathcal{V}_r - b)^3} - \frac{1}{2(\mathcal{V} - b)^2} - \frac{b}{3(\mathcal{V} - b)^3}\right] \\
& + 4A_4\left[\frac{1}{3(\mathcal{V}_r - b)^3} + \frac{b}{4(\mathcal{V}_r - b)^4} - \frac{1}{3(\mathcal{V} - b)^3} - \frac{b}{4(\mathcal{V} - b)^4}\right] \\
& \left. + 5(A_5 + B_5 T + C_5 e^{-KT})\left[\frac{1}{4(\mathcal{V}_r - b)^4} + \frac{b}{5(\mathcal{V}_r - b)^5} - \frac{1}{4(\mathcal{V} - b)^4} - \frac{b}{5(\mathcal{V} - b)^5}\right]\right\} \\
& - 4B_4 T\left[\frac{1}{3(\mathcal{V}_r - b)^3} + \frac{b}{4(\mathcal{V}_r - b)^4} - \frac{1}{3(\mathcal{V} - b)^3} - \frac{b}{4(\mathcal{V} - b)^4}\right] \\
& + (A_6 + B_6 T)\frac{1}{\alpha}\left[e^{\alpha \mathcal{V}}(\alpha \mathcal{V} - 1) - e^{\alpha \mathcal{V}_r}(\alpha \mathcal{V}_r - 1)\right] + T\left\{R \ln\left(\frac{\mathcal{V} - b}{\alpha \mathcal{V}_r - b}\right)\right. \\
& - (B_2 - KC_2 e^{-KT})\left(\frac{1}{\mathcal{V} - b} - \frac{1}{\mathcal{V}_r - b}\right) - \frac{B_3 - KC_3 e^{-KT}}{2}\left[\frac{1}{(\mathcal{V} - b)^2} - \frac{1}{(\mathcal{V}_r - b)^2}\right] \\
& \left. - B_4\left[\frac{1}{3(\mathcal{V} - b)^3} - \frac{1}{3(\mathcal{V}_r - b)^3}\right] - \frac{B_5 - KC_5 e^{-KT}}{4}\left[\frac{1}{(\mathcal{V} - b)^4} - \frac{1}{\mathcal{V}_r - b)^4}\right] + \frac{B_6}{\alpha}(e^{\alpha \mathcal{V}} - e^{\alpha \mathcal{V}_r})\right\} \qquad (4.3)
\end{aligned}
$$

Subsonic inflow boundary conditions often use an isentropic condition. The equation for entropy for CF_4 gas is equation (4.4)

$$
\begin{aligned}
S - S_r = {} & a_4 \ln \frac{T}{T_r} + b_4(T - T_r) + \frac{c_4}{2}(T^2 - T_r^2) + \frac{d_4}{3}(T^3 - T_r^3) \\
& + K(e^{-KT} - e^{-KT_r})\left[\frac{C_2}{\mathcal{V}_r - \hat{b}} + \frac{C_3}{2(\mathcal{V}_r - \hat{b})^2} + \frac{C_5}{4(\mathcal{V} - r - \hat{b})^4}\right] \\
& + R \ln\left(\frac{\mathcal{V} - \hat{b}}{\mathcal{V}_r - \hat{b}}\right) - (B_2 - KC_2 e^{-KT})\left(\frac{1}{\mathcal{V} - \hat{b}} - \frac{1}{\mathcal{V}_r - \hat{b}}\right) \\
& - \frac{B_3 - KC_3 e^{-KT}}{2}\left[\frac{1}{(\mathcal{V} - \hat{b})^2} - \frac{1}{(\mathcal{V}_r - \hat{b})^2}\right] \\
& - \frac{B_5 - KC_5 e^{-KT}}{4}\left[\frac{1}{(\mathcal{V} - \hat{b})^4} - \frac{1}{(\mathcal{V}_r - \hat{b})^4}\right] \\
& - B_4\left[\frac{1}{3(\mathcal{V} - \hat{b})^3} - \frac{1}{3(\mathcal{V}_r - \hat{b})^3}\right] + B_6\left(\frac{e^{\alpha \mathcal{V}}}{\alpha} - \frac{e^{\alpha \mathcal{V}_r}}{\alpha}\right) \qquad (4.4)
\end{aligned}
$$

Constants, A_i, B_i, C_i, K, and $\hat{b}$ used in equations (4.2), (4.3), and (4.4) are listed in

Table 2. Solving these equations for variables other than those for which they are written obviously requires an iterative procedure. Analysis experience in the present research indicates that the computational expense in iterating these equations at every time step is considerable when compared to interpolation from previously generated data. A computer program developed by Hunt and Boney [12] for use in data reduction at the Hypersonic CF_4 Tunnel is used to generate the tabular information.

5 Boundary Conditions

Four sets of boundary conditions are needed when solving the Navier-Stokes equations in an axisymmetric system — upstream, downstream, wall and centerline. An initial condition is also required. Details of these conditions are presented in this section. For discussion of the boundary conditions used in the spacial marching techniques of the MOC/BL design and analysis, see sections A.1.2, A.1.3 and A.2.1-A.2.3.

5.1 Centerline Boundary Conditions

With internal axisymmetric flows, all disturbances are created by the wall and propagate along characteristic lines to ultimately impinge upon the centerline. This phenomenon emphasizes the importance of a robust centerline boundary condition. Of course the centerline boundary condition must be mathematically and physically accurate, but with the possibility of the existence of oblique shock waves, it must also be numerically stable.

The main difficulty in treating the axisymmetric centerline is the singularities existing in the source term of the Navier-Stokes equation set and in the Jacobian of the numerical transformation for $y = 0$. The singularities restrict integration from proceeding normally on the centerline. The fourth term of Navier-Stokes equation, eq. (2.3), contains the apparent singularity for $y = 0$. It is obvious, however, that

this singularity cannot physically exist in axisymmetric flows. In fact, it can be removed by taking the limit of the entire equation set as y approaches zero which includes a simple application of L'Hopital's rule. However, even with the apparent physical singularity removed from the Navier-Stokes equations, integration is still restricted on the centerline. Recall that the Jacobian for the transformation is

$$J = 1/(x_\eta y_\xi - x_\xi y_\eta).$$

Considering the transformation implied by Figure 3.1, it is obvious that x_η is zero for all points; x does not change with respect to the η direction. When one remembers the symmetry condition that is basic to the axisymmetric system, it becomes clear that regardless of the distribution of y in the η direction y_η is also zero on the centerline. Therefore, J is singular and integration cannot take place on the centerline in the transformed plane.

Presently, the centerline boundary condition is treated using the symmetry condition existing in the original Navier-Stokes solver of reference [11]. The actual centerline is not in the domain, but is surrounded on either side by a grid line thus avoiding the singularity of J and the Navier-Stokes equation set. The governing equations are integrated on points above the centerline and the properties are

reflected to the points below the centerline to exploit symmetry, as follows:

$$\rho_{x,1} = \rho_{x,2}$$

$$\rho u_{x,1} = \rho u_{x,2}$$

$$\rho v_{x,1} = -\rho v_{x,2}$$

$$\rho E_{x,1} = \rho E_{x,2}.$$

However, solutions using this technique are often characterized by oscillations in flow properties at the centerline, especially where high gradients exist such as shock waves hitting the centerline or flow through the throat section of a nozzle. Although the numerical accuracy is not likely to be maintained through a strong shock hitting the centerline, this is acceptable since a nozzle with shock waves is of little interest in this research.

5.2 Subsonic Inflow Boundary Conditions

Unlike supersonic inflow boundary conditions, which are generally held constant at some freestream condition, the subsonic inflow boundary condition influences and is influenced by the downstream conditions. This feedback relationship is difficult to accurately model. Characteristic Theory indicates that three properties be specified on the subsonic inflow boundary. A fourth property is extrapolated from the interior.

For this study, S_o, h_o and flow angularity are specified while P is linearly extrapolated from the interior of the flow. Entropy on the inflow face is held constant at, S_o, the stagnation entropy. P and S_o are used to solve for the remaining thermo-

dynamic variables. The isentropic condition allows the following adiabatic energy equation to be used to calculate the V, velocity magnitude.

$$H_o = h + \frac{1}{2}V^2$$

The flow angularity and this velocity magnitude specify the u and v velocities.

5.3 Wall and Supersonic Outflow Boundary Conditions

Extrapolation is used for both the wall and outflow boundaries. The supersonic outflow boundary depends only upon upstream conditions. All properties across the entire outflow boundary are obtained in this way, so there are inaccuracies in the boundary layer region near the wall where the flow is no longer supersonic.

At the wall, the temperature is known and the no slip condition is used, therefore extrapolation of p from the interior fixes the thermodynamic condition along the wall. Boundary layer theory, which assumes that the pressure is constant across a thin boundary layer, gives support to the use of extrapolation at the wall.

5.4 Initial Conditions

A quasi-two-dimensional isentropic expansion with constant mass flow rate is used as the starting solution. Flow quantities at the face of the grid are known from the previously analyzed section or are specified in the case of subsonic inflow to be the subsonic solution to the standard isentropic flow equations. For the subsonic case, the quantities are kept constant across the inflow plane. The massflow rate

is calculated for the inflow plane and kept constant at this value for all subsequent grid locations.

With the geometry of the nozzle and hence the area ratio, A/A^* known, Newton's method is applied to equation (5.1) to determine the Mach number at each grid location.

$$\left(\frac{A^*}{A}\right)_i = \left(\frac{\gamma+1}{2}\right)^{\frac{\gamma+1}{2(\gamma-1)}} M_i \left(1+\frac{\gamma-1}{2}M_i^2\right)^{-\frac{\gamma+1}{2(\gamma-1)}} \tag{5.1}$$

The isentropic flow relationship, eqn. (5.2), is used in conjunction with the reservoir temperature to calculate T_i, where i represents axial grid location.

$$\frac{T_o}{T_i} = 1+\frac{\gamma-1}{2}M_i^2 \tag{5.2}$$

The velocity vector is kept parallel to the axis of symmetry for the initial solution with a magnitude calculated from the speed of sound and M_i with eqn. (5.3).

$$u_i = M_i a_i = M_i\sqrt{\gamma R T_i} \tag{5.3}$$

Finally the thermodynamic state is fixed by the massflow rate equation, (5.4), and equation of state, eqn. (5.5).

$$\rho_i = \frac{\dot{m}}{u_i A_i} \tag{5.4}$$

$$P_i = \rho_i R T_i \tag{5.5}$$

6 Results and Discussion

The MOC/BL design approach requires a specified wall temperature and centerline Mach number distribution in the initial expansion region (between points A and B of Fig. 1.3). The wall temperature distributions for the air nozzle and the nitrogen nozzles are based on a heat transfer study done on the wall of a Mach 17 hypersonic wind tunnel nozzle by Sverdrup and are plotted in Fig. 6.0. Notice that the wall temperatures in Fig. 6.0 start at about $100°R$ to $200°R$ below the stagnation temperature at the throat and rapidly decrease to some specified constant temperature. The decrease follows the behavior of the freestream. The choice of AB Mach number distribution is generally linear with the exception of the $N_2 - 17$ nozzle.

The general approach for the Navier-Stokes analysis of the present designs was to divide the nozzle into short sections and analyze them separately. Attempts to load an entire nozzle into a single run failed because the CFL stability condition near the throat was drastically different than that near the nozzle exit. This was due to the large gradients in the throat section compared to those near the exit. Since the Navier-Stokes code used here has no capacity for adjusting the CFL condition at different grid locations the only alternative was to analyze the nozzle in shorter sections. Each time a new section of the nozzle was analyzed, the flow domain was overlapped to account for the upstream propagation of information in

the boundary layer region and to reduce the influence of the extrapolation at the outflow boundary on the final solution. In areas of high wall curvature and high axial gradients, such as near the throat and inflection point, 0.1 inch x grid resolution was used. Downstream of the inflection point where the pressure gradients are low, 0.2 inch or more x grid spacing was used. The first section (throat section) employed the subsonic inflow boundary condition discussed in section 5.2.

6.1 Mach 6 Air Nozzle

The Experimental Aerodynamics Branch of NASA Langley is in possession of a nozzle from a dismantled Mach 10 air wind tunnel. Instead of scraping the nozzle, it was decided to use it as the raw casting for the nozzle of an undeveloped Mach 6 wind tunnel. The new contoured nozzle must fit inside the existing casting which is 1 inch thick for the majority of its length. The total length is fixed as is the nozzle exit diameter, and it must deliver uniform Mach 5.95 flow.

The contour was designed for perfect gas, $\gamma = 1.4$ since air behaves perfectly at and below the stagnation conditions, $P_o = 45$ *psia*, $T_o = 1260°R$. The wall temperature distribution was fixed to that shown in Fig. 6.0 and the AB Mach number distribution was specified as linear. Several MOC/BL iterations were performed where the maximum turning angle, θ_{max} was varied until the contour fit inside the tolerance and exhibited the design exit diameter of 14.4 inches. At this point θ_{max} was adjusted to 12° so that a minimum of metal will be removed from the existing nozzle. The total length of the nozzle at this point was 66 inches while the nozzle

casting is 76 inches. So, before adding the boundary layer correction for the final iteration, a straight, horizontal 10 inch long section was added to the characteristic (inviscid) coordinates and the edge conditions were kept constant. The final contour is compared to the original contour in Fig. 6.1.1 and is tabulated in Table 3. The section numbers indicate the three nozzle sections and where they bolt together. A minimum of 0.0054 inches and a maximum of 0.4524 inches of metal will be removed. Fig. 6.1.2 shows the inviscid coordinates and boundary layer edge in relation to the final contour. Calculations of δ, based on the velocity profile, predicted eleven inches of isentropic core at the nozzle exit.

The Navier-Stokes analysis of the air nozzle was done in 8 sections, each with 0.1 inch longitudinal spacing and 51 points in the radial direction. The final grid network was 769 x 51 points for the entire nozzle. Calculated static pressure and Mach number contours are shown in Fig. 6.1.3 and Fig. 6.1.4 respectively. The Mach 6 contour of Fig. 6.1.4 clearly shows the formation of the desired uniform flow core along the final Mach line corresponding to line DE of Fig. 1.3. The horizontal portion of the Mach 6 contour near the nozzle wall shows the straight 10 inch section added to the inviscid coordinates of the nozzle. As expected, the flow in this region remained fairly uniform. While the design is for Mach 5.95 the Navier-Stokes solution predicted Mach 6.06 flow across the nozzle exit plane, a 1.85% difference. Corresponding to this, Fig. 6.1.3 shows the static pressure in the uniform flow region oscillating about 185 Pa which is 10.5% lower than the

design pressure of 207 Pa. A small compression wave is seen in Fig. 6.1.3 starting at the wall and impinging upon centerline about halfway down the nozzle. This point on the centerline corresponds to point D of Fig. 1.3 and any disturbance occurring here can be traced back along the characteristic CD to emanate from the inflection point, C. Directly downstream of the compression on the centerline, the flow expands upward into the core region causing some oscillations of static pressure and Mach number. The downstream effects of this compression/expansion appear to damp out as Fig. 6.1.5 shows the exit plane Mach number profile where the variation is within 0.25%. Fig. 6.1.6 shows the centerline ratio $(P/P_o)_{NS}$ compared to design. The rise in pressure ratio near $x = 35$ inches is evidence the compression wave hitting the centerline. Again, the oscillations in $(P/P_o)_{NS}$ are damped to a minimum well before the exit.

Since all total pressure measurements in supersonic wind tunnels are taken behind behind normal shock waves, it is important to examine the flow quality behind a shock. Exit plane data was used as upstream conditions for ideal gas normal shock relations to get conditions downstream of a normal shockwave. Fig. 6.1.7 shows the profile of the exit plane ratio, $(P_o)_y/P_x$, where y denotes downstream of a normal shock and x is upstream. The variation across the core is within 0.46% and the mean value of $(P_o)_y/P_x$ is 4.1% higher than design. The effects of oscillations in upstream static pressure is evident in Fig. 6.1.8 showing the downstream total pressure $(P_o)_y$ profile across the core with variations up to 1.16%. Again these small

variations across the profiles are a result of the compression/expansion activity at and beyond the design point, D. The mean value of $(P_o)_y$ across the nozzle exit plane is approximately 6.5% lower than design. This result is consistent since the nozzle was predicted to be overexpanded which should cause the normal shock to be stronger and yield lower total pressure behind the shockwave. It is the 10.5% lower P_s that makes the ratio, $(P_o)_y/P_s$, 4.1% higher than design.

Fig. 6.1.9 shows the MOC/BL design wall pressure compared to the Navier-Stokes wall pressure. Recall that the MOC/BL theory assumes zero normal pressure gradients in the boundary layer, so the solid line actually represents the behavior of static pressure during the isentropic expansion of ideal air from Mach 1 to Mach 5.95. The pressure is predicted to be about 12.5% lower than design at the nozzle exit. In fact, after about $x = 20$ inches, the Navier-Stokes wall pressure is consistently lower than design. Recall however that the nozzle is predicted to be overexpanded by about 10.5% in static pressure. The remaining 2% difference in wall pressure at the nozzle exit may be attributed to a non-zero normal pressure gradient across the boundary layer, or even a compilation of numerical errors made in the design procedure and Navier-Stokes analysis. An indication of the magnitude of the numerical error in the Navier-Stokes solution can be seen in Fig. 6.1.10. The plot shows a 1.12% increase in massflow rate from the nozzle inlet to the outflow plane. Since this behavior clearly violates the law of conservation of mass, the errors must be attributed to numerics and may have influenced the solution.

The Navier-Stokes analysis predicted that the Air nozzle contour expands to 10.5% below design static pressure and 1.85% above M_D. In addition, the nozzle is characterized by a small oblique compression wave. Oscillations produced by its subsequent expansion off the centerline damp out before the exit. Overall agreement between the design and Navier-Stokes analysis of the Mach 6 air nozzle is good. The final contour fits inside the prescribed tolerance enabling its manufacture to proceed. The design exhibits all of the exit flow requirements within a few percent variance.

6.2 $N_2 - 13$ and $N_2 - 17$ Nozzles

The $N_2 - 13$ and $N_2 - 17$ nozzles were designed and analyzed using the same MOC/BL and Navier-Stokes codes used for the Air nozzle. The codes were coupled with a set of isentropic expansion and thermodynamic property tables for thermally perfect nitrogen. Design stagnation conditions for the $N_2 - 13$ and $N_2 - 17$ nozzles are respectively $P_o = 4000$ *psia*, $T_o = 3400°R$ and $P_o = 4000$ *psia*, $T_o = 3000°R$. For these stagnation conditions in the absence of any strong compression or shock wave, nitrogen is non-reacting and intermolecular forces are insignificant.

Both contours were designed for $\theta_{max} = 12°$. The AB Mach number distribution is linear for the Mach 13.5 case and a third order polynomial for the Mach 17 case. The third order polynomial was chosen to lengthen the initial expansion region in order to maintain vibrational equilibrium. The wall temperature distributions were fixed at those illustrated in Fig. 6.0.

The usual iteration procedure was performed in order to determine the proper

displacement thickness to yield the design exit radius. The final nozzle contours are illustrated in Figs. 6.2.1 and 6.2.2 and tabulated in Table 4 and Table 5. Figs. 6.2.1 and 6.2.2 show the relation of the characteristic coordinates and boundary layer edge to the actual nozzle contours. The boundary layer edge profile, calculated based on velocity rather than on density, predicted 9.5 inches of isentropic core flow at the nozzle exit for the $N_2 - 13$ nozzle and 8.8 inches for $N_2 - 17$. However, a pitot pressure survey across the exit plane flow would not necessarily predict the same amount of core flow. Because the pitot tube essentially measures changes in entropy across the profile, it will detect the edge of the wall entropy layer whether the increase in entropy is due to the velocity gradient or the thermal gradient. Thick thermal boundary layers are characteristic of both the nitrogen nozzles. For these nozzles, the wall temperature at the exit, $600°R$, is very high compared to the freestream temperature of equilibrium nitrogen at Mach 13.5 or Mach 17. Under the assumption of constant pressure boundary layer profiles, the high temperatures at the wall push the mass away from the wall. The larger the temperature gradient, the more the density profile is pushed away from the wall. So for the nitrogen nozzles, δ based on this type of density profile will be larger than δ based on the velocity profile such as those of Figs. 6.2.1 and 6.2.2. In fact, consideration of the thermal boundary layer in the case of $N_2 - 13$ predicted the isentropic core to be almost an inch smaller than when δ is based on the velocity profile alone.

Near $x = 105$ inches on the $N_2 - 17$ contour of Fig. 6.2.2, a small discontinuity is

visible. This numerical error was smoothed out using a least squares fit by trial and error and is not evident in Fig. 6.2.3 which shows the smoothed $N_2 - 17$ contour alongside its first and second derivative. Smoothing of the $N_2 - 13$ contour was unnecessary as the first and second derivatives of the raw design data illustrate in Fig. 6.2.4. It is obvious that discontinuities such as that pointed out in Fig. 6.2.2 could cause oblique shock waves to develop. However, it is not so clear as to how sensitive flows such as these are to wall smoothness. The approach here was to provide contours that are smooth in the first and second derivative in hopes to avoid the development of shockwaves.

Navier-Stokes analysis of the $N_2 - 13$ nozzle was done in 6 sections. One tenth inch axial grid spacing was used for the first 9 inches of the nozzle. The same basic grid structure was used in the analysis of the $N_2 - 17$ nozzle.

Figs. 6.2.5 and 6.2.6 shows the calculated static pressure and Mach number contours for the $N_2 - 13$ nozzle. The behavior of pressure contours show evidence of a series of oblique compression waves. The small *bubble* contours on the centerline after point D are relative lows in pressure. In between these are regions of compressing flow due to the compression waves from the upstream wall and impinging upon the expanding centerline. The source of the first compression can be traced back to just upstream of the inflection point. These compression waves are expanded off the centerline to contaminate the downstream flow. In order to clarify the behavior of the pressure contours near the centerline, the centerline ratio, P/P_o is compared to

design in Fig. 6.2.7. The alternating compression/expansion is visible. The Navier-Stokes solution follows the design closely for only the first 4 to 5 inches. The critical inflection point is located at $x = 5.1$ inches. $(P/P_o)_{NS}$ is consistently higher than design downstream of the inflection point.

The Navier-Stokes solution includes implicitly a representation of δ^*. That is, there exists a place within the Navier-Stokes boundary layer region where the characteristic waves are reflected back into the mean flow or cancelled. The assumption in the boundary layer corrections was that properties remain constant at the boundary layer edge values down into the boundary layer until δ^* is reached. Hence in the MOC solution, the slopes of the Mach lines between δ and δ^* are assumed to remain constant at each boundary layer profile. In the Navier-Stokes solution, especially where the boundary layers get thick, this assumption may not be correct. Characteristic waves entering the boundary layer may curve toward the wall as the Mach number decreases. Therefore it is possible that the waves in the Navier-Stokes solution curved toward the wall between δ and δ^* and reflected or cancelled in a location that was further from the wall than assumed in the design. This would have two consequences. With the two solutions agreeing well near the throat, thus fixing the throat area, the larger δ^*_{NS} (effective δ^* calculated by the Navier-Stokes solution) reduces the area ratio for the Navier-Stokes solution thus increasing the pressure and reducing the Mach number. This would explain the behavior of the centerline pressure ratio in Fig. 6.2.7, which never reaches the design expansion.

The second consequence is the possibility of δ^*_{NS} growing large enough to turn the mean flow into itself to form the oblique compression waves seen forming near the inflection point.

The above explanation, if accurate, could also explain much of the noted behavior of the Air nozzle. Specifically, the way the nozzle was predicted to expand beyond design. The above argument might hold with the exception that the waves reflected or cancelled at a point in the boundary layer closer to the wall thus increasing the effective area ratio. If this scenario is the case, then it indicates a serious limitation for which the present MOC/BL design method does not account. Unfortunately, the present study is not well suited for the determination of the accuracy of this scenario as this study was originally conceived as a development project rather than a research project.

Two contours were designed for Mach 17. The first was designed for a wall temperature distribution that qualitatively followed the behavior of the CF_4 curve of Fig. 6.0 only starting at $3200°R$. Later, wall temperature data from a heat transfer study on a Mach 17 nozzle was obtained and used in the design of a second nozzle contour. Wall temperature distributions used in the Air and $N_2 - 13$ designs were also based on this data. In both $N_2 - 17$ nozzles the AB Mach number distribution followed a third order polynomial.

The static pressure contours and Mach number contours for the first $N_2 - 17$ design are in Figs. 6.2.8 and 6.2.9. Again a series of compression waves starting from

around the inflection point impinge upon the centerline just beyond the design point D. The centerline ratio $(P/P_o)_{NS}$ in Fig. 6.2.10 shows the expansion interrupted just beyond the design point by the strong compression. The fact that the nozzle expanded to and beyond Mach 17.1 indicates that the source of the compression wave is just downstream of the inflection point. The shock wave in this case is strong enough to cause the flow to go from the Mach 17.1 to Mach 15 in just 10 inches. Since the overall objective is to design isentropic nozzles, the Navier-Stokes solution was stopped when this shock wave was discovered.

Dr. A. Kumar of NASA Langley also analyzed this contour and the centerline results are given in Fig. 6.2.11. Kumar's analysis of the same contour used the same Navier-Stokes code as the above cases, but with a different source for the thermodynamics. The results of Kumar's case and that of figure 6.2.10 are practically identical for the behavior of the centerline pressure ratio. The Mach number and pressure contours shown in Figs. 6.2.8 and 6.2.9 are from Kumar's run since the analysis of the first $N_2 - 17$ contour was terminated in the presence of the compression wave.

Analysis results for the second $N_2 - 17$ contour are even further from design than for the previous contour. The most significant difference between the two cases is that the first contour was predicted to expand to Mach 17.1 and then shock down dramatically, but the second case never reached Mach 17. Fig. 6.2.12 shows the ratio $(P/P_o)_{NS}$ for the second case. Note that the expansion slows down before the

design point and almost levels off until an obvious compression wave increases the pressure near $x = 40$ inches. This indicates that the flow was constricted upstream of the inflection point producing a series of weak compressions. Now since the mean flow is not moving at design conditions the shape of the nozzle wall downstream of this constriction — where the nozzle begins to turn the flow — is not correctly contoured to cancel the characteristic waves. The Mach number is lower than design so the waves have a steeper Mach angle and thus pile up to form a compression wave.

Overall agreement between the design and Navier-Stokes analysis of these two nozzles for the Hypersonic Nitrogen tunnel is poor. The analysis of these contours reveals a series of compression waves emanating near the inflection point, impinging upon the centerline, contaminating and increasing the entropy of the mean flow region.

Two characteristics common to all Navier-Stokes analyses in this report are the existence of compression waves and their apparent source. In the Mach 6 air nozzle the wave is very weak so that nonuniformities produced by its expansion from the centerline are damped. For the $N_2 - 13$ and $N_2 - 17$ nozzles the wave is stronger and the flow is unable to recover from its violent expansion off the centerline. The catastrophic downstream effects of the compression wave is apparently amplified with increased Mach number. The source of the compression waves has been traced back in all cases to emanate from near the inflection point. This happens because, until the inflection point is reached, the nozzle wall is diverging so that it would

take large errors in the boundary layer correction to create a strong compression wave. But once the inflection point is reached the nozzle wall is already beginning to decrease in slope, so it would take a smaller error in δ^* to create a compression wave. Therefore, if the cause of these compressions is based in errors or limitations in current δ^* calculations for these high Mach number nozzles, any compression wave would most likely appear near the inflection point or downstream. The only explanation offered thus far as to how the compressions are formed has targeted assumptions made in the design. The concept here has been outlined earlier in this section and in Chapter 1 and will not be repeated. But there are other possible scenarios. The Navier-Stokes analysis, being rather expensive, resolved the boundary layer with 20 to 25 points at each station compared to the boundary layer code used in the design which uses 100 points per station. The low resolution used in the Navier-Stokes analysis may not be adequate for internal flows where boundary layer thickness is so critical. The resolution used in the x direction was no greater than 0.1 inch. Fig. 6.2.13 illustrates how low x resolution in the Navier-Stokes analysis grid can alter the shape of the nozzle contour and even move the inflection point, both of which could aid in the formation of a compression wave. As the original scope of this study was developmental in nature, there is insufficient information to determine which, if any, of these proposals contributed to the compression waves and underexpanded conditions of the present nozzles. Further study is needed to determine whether these features are introduced by the Navier-Stokes analysis or if

they actually represent a limitation of the current design methods.

6.3 CF_4 Nozzle

For the design of the CF_4 nozzle, the same MOC/BL codes were again used only coupled with a more complex set of thermodynamic and expansion tables. The design stagnation conditions are $P_o = 1600$ *psia*, $T_o = 1260°R$. Since virial effects of CF_4 are significant throughout the pressure range considered here, the standard gas law, which is used implicitly throughout most Navier-Stokes solvers, was replaced by the thermodynamic tables in the computer codes. The tables are essentially a set of temperature tables at a range of different pressure settings, which allow thermodynamic properties to be calculated as functions of any other two thermodynamic properties. The wall temperature distribution was calculated using an equation in [6] which was in turn based on experimental data from the existing CF_4 nozzle. The centerline Mach number distribution was specified as linear. The design proceeded as before with the final contour converging at the design exit radius of 10 inches at a length of 98 inches. The contour is shown in Fig. 6.3.1. The first and second derivative of the raw design data revealed some radical slope changes, but were eliminated by some minor least squares smoothing. The first and second derivatives of the smoothed contour are illustrated Fig. 6.3.2. The final smoothed contour is tabulated in Table 6.

The Navier-Stokes analysis of the CF_4 nozzle was unsuccessful. After months of modifying the original code for a virial gas and the table look-up scheme and debug-

ging, the resulting Navier-Stokes code was numerically unstable for virtually any CFL condition and damping coefficient. Different centerline and inflow boundaries were tried without success. No success was obtained by analyzing the same contour under the perfect gas assumption for a gas of $\gamma = 1.1$. The solution diverged in all cases tried.

Design of the Mach 6 Air nozzle of section 6.1 and design of the CF_4 contour followed identical procedures and used the same computer codes. The two nozzles were designed for the same exit Mach number, wall temperature distribution, AB Mach number distribution, and reservoir temperature. The major differences between the two cases are P_o and the working gas.

Thompson and Sutton [6] showed that the MOC/BL approach works well for CF_4 when they conducted a MOC/BL analysis and preliminary redesign of the existing CF_4 nozzle in an attempt to characterize the centerline disturbance of figure 2. They conducted the MOC/BL analysis of the nozzle at $P_o = 2252$ *psia*, $P_o = 1742$ *psia* and $P_o = 1515$ *psia*. Comparisons of exit plane total pressure ratios computed by the MOC/BL procedure to profiles measured experimentally showed good qualitative agreement. In areas not in the region of the centerline disturbance, the profiles showed good quantitative agreement. Since the MOC/BL philosophy worked well for the Thompson study, which modeled CF_4 gas in the same reservoir pressure range as the presently designed contour, the philosophy should therefore be applicable to the present CF_4 nozzle design. Furthermore, if the reservoir pressure and working

gas of the CF_4 nozzle design do not undermine the philosophy behind the MOC/BL approach and these are the only significant differences between this design and the Mach 6 air nozzle design, then the satisfactory results of the air nozzle analysis may be useful in inferring confidence in the present CF_4 nozzle design.

However, inherent in the equations of motion are terms involving M and γ where low γ has similar qualitative effects as high M. For example, in the simple case of one-dimensional isentropic flow of ideal gases the following relations are valid.

$$\frac{P_o}{P} = \left(1 + \frac{\gamma - 1}{2} M^2\right)^{\frac{\gamma}{\gamma - 1}}$$

$$\frac{\rho_o}{\rho} = \left(1 + \frac{\gamma - 1}{2} M^2\right)^{\frac{1}{\gamma - 1}}$$

Applying these equations to Mach 6, $\gamma = 1.1$ (idealization of CF_4 case) and Mach 17, $\gamma = 1.4$ (idealization of $N_2 - 17$ case),

Mach	γ	P_o/P	ρ_o/ρ
6	1.4	$1.58x10^3$	192.5
6	1.1	$8.29x10^4$	$2.96x10^4$
17	1.4	$1.56x10^6$	$2.65x10^4$
17	1.1	$1.20x10^{13}$	$7.75x10^{11}$

The results for the two cases are very close for the total density equation and comparable for the total pressure equation. Since these equations are essentially a subset of the Navier-Stokes equations, their effects are implicitly included in the Navier-Stokes equations. This crudely illustrates the concern for putting overdue confidence in the CF_4 design by comparisons to the Air nozzle case. It is possible

that the apparent amplification of the compression wave in the analysis of the preceeding nitrogen nozzles could take place in the CF_4 nozzle only through a decreased γ rather than an increased Mach number.

7 Conclusions

1. The Mach 6 air nozzle is designed to fit all design constraints. The Navier-Stokes analysis of the design reveals a weak compression wave and predicts the nozzle to expand slightly beyond design. Overall however, the Navier-Stokes solution shows good quantitative agreement with the design conditions.

2. The Mach 13.5 nozzle for the Hypersonic Nitrogen Tunnel is designed to fit all design constraints. The Navier-Stokes analysis shows poor agreement with the design flow conditions. The nozzle is predicted to be underexpanded and has a series of oblique compression waves contaminating the flow.

3. Two Mach 17 nozzle contours are designed for the Hypersonic Nitrogen Tunnel to fit all design constraints. The Navier-Stokes solutions show poor agreement with the design flow conditions. Both contours are predicted to have oblique compression waves. One contour expands to design conditions on the centerline before the compression waves shock the core down and the other is predicted to be underexpanded.

4. The Mach 6 CF_4 nozzle for the Hypersonic CF_4 Tunnel is designed to fit all design constraints. The Navier-Stokes analysis of the nozzle contour is unsuccessful because of numerical instabilities in the computer code. Because the effects of low γ on nozzle flows are suspected to be similar to those of

high Mach number (the $N_2 - 13$ and $N_2 - 17$ cases), the flow in this nozzle may be characterized by a compression wave from the inflection point of such strength as to shock down the nozzle.

5. The source of the compression waves seen in all Navier-Stokes solutions emanating from near the inflection point of the nozzles is not precisely determined. If the apparent amplification of the downstream effects of the waves with Mach number can be attributed to a limitation in the current nozzle design methods rather than a numerical limitation in the Navier-Stokes analysis of high speed internal flows, then the present state of MOC/BL nozzle design is not adequate to give reliable contoured nozzle designs at higher Mach numbers.

6. If such a limitations exists then it appears to be in between Mach 8 and Mach 12. The current methods are shown here to work adequately for Mach 6 and in an unpublished study for Mach 8. Problems have been recorded elsewhere at Mach 12 and in this study at Mach 13.5 and Mach 17.

7. Further research is required in the area of high Mach number MOC/BL contoured wind tunnel nozzle design in order to determine whether the apparent limitations of the current techniques are rooted in the design methods or were caused by the Navier-Stokes analysis.

8 Recommendations

This project was originally conceived as a development project — specifically, to develop hypersonic wind tunnels to meet the standard of high quality flow. Over the course of the effort many areas within the nozzle design discipline have been discovered where limitations in the current methods are apparent. Some serious and basic research is needed in this area. The following is a partial list as to where the author feels this research should be concentrated.

1. Develop a Navier-Stokes solver specifically designed for internal flow problems, particularly axisymmetric geometries. This code should have the following characteristics:

   - adjustable CFL condition according to gradients within the flow so that entire nozzles can be loaded into a single run.
   - use of effective γ's and compressibility factor, Z, so that equilibrium effects and real gas virial effects can be easily included and updated every 5 to 10 time steps.
   - use of finite volume scheme instead of finite difference scheme. The author feels that the volumetric approach is a more sophisticated way to approach the axisymmetric centerline problem.

- research is needed to provide a reliable, accurate subsonic inflow boundary condition or starting solution for these and other flows.

2. Perform extensive parametric studies using MOC/BL nozzle design and Navier-Stokes analysis to gain basic understanding of how design parameters effect nozzle flow and to get a better understanding of the limitations of the MOC/BL approach.

3. If further research concludes that the current MOC/BL techniques become inaccurate at some limiting Mach number, research should proceed in developing an alternative design algorithm. A spacial marching technique that can be used in conjunction with the Parabolized Navier-Stokes equations should be investigated.

References

[1] Trimmer, L. L. and Voisinet, R. L., "The Optimum Hypersonic Wind Tunnel," AIAA Paper 86-0739-CP, March 1986.

[2] Clark et al., "Recent Work in Flow Evaluation and Techniques of Operations for the Langley Hypersonic Nitrogen Facility," Fifth Hypervelocity Techniques Symposium, March 1967.

[3] Miller, C. G. and Smith, F. M., "Langley Hypersonic Facilities Complex – Description and Application," AIAA Paper 86-0741-CP, March 1986.

[4] Arrington, J. P. et al., "Longitudinal Characteristics of Several Configurations at Hypersonic Mach Numbers in Conical and Contoured Nozzles," NASA TN D-2489, September 1964.

[5] Midden, R. E. and Miller, C. G., "Description of the Langley Hypersonic CF_4 Tunnel," NASA TP-2384, March 1985.

[6] Thompson, R. A. and Sutton K., "Computational Analysis of the Langley Hypersonic CF_4 Tunnel Nozzle and Preliminary Redesign," NASA TM-89042, March 1987.

[7] Johnson, C. B. et al., "Real-Gas Effects on Hypersonic Nozzle Contours with a Method of Calculation," NASA TN D-1622, April 1963.

[8] Johnson, C. B. and Boney, L. R., "A Method for Calculating a Real-Gas Two-Dimensional Nozzle Contour Including the Effects of Gamma," NASA TM X-3243.

[9] Anderson, E. C. and Lewis C. H., "Laminar or Turbulent Boundary-Layer Flows of Perfect Gases or Reacting Gas Mixtures in Chemical Equilibrium," NASA CR-1893.

[10] Zucrow, M. J. and Hoffman, J. D., **Gas Dynamics, Volume 2: Multidimensional Flow**, John Wiley & Sons, Inc., 1977.

[11] Kumar, A., "Numerical Analysis of the Scramjet Inlet Flow Using Two Dimensional Navier-Stokes Equations," AIAA Paper 81-0185, January 1981.

[12] Hunt, J. L. and Boney, L.R., "Thermodynamic and Transport Properties of Gaseous Tetraflouromethane in Chemical Equilibrium," NASA TN D-7181, 1973.

[13] White, Frank M., **Viscous Fluid Flow**, McGraw-Hill Book Company, New York, 1974.

[14] Baldwin, B.S. and Lomax, H., "Thin Layer Approximation and Algebraic Model for Seperated Turbulent Flows," AIAA Paper 78-257, January, 1978.

[15] Anderson, D. A., Tannehill, J.C, Pletcher R. H., **Computational Fluid Mechanics and Heat Transfer**, Hemisphere Publishing Corporation, New York, 1984.

Appendices

A Method of Characteristics Applied to Nozzles

The equations governing axisymmetric, irrotational, steady, supersonic flowfields, equations (A.1) and (A.2), are hyperbolic, quasi-linear partial differential equations and can therefore be solved using the Method of Characteristics (MOC). In a hyperbolic system, there exist characteristic curves (characteristics) along which the governing partial differential equations can be manipulated into ordinary differential equations called *compatability equations*. Across characteristics, flow properties may have discontinuous derivatives while the property itself remains continuous. For these equations,

$$\left(1-\frac{u^2}{a^2}\right)u_x-\left(\frac{uv}{a^2}\right)u_y+\left(1-\frac{v^2}{a^2}\right)v_y=-\frac{v}{y} \tag{A.1}$$

$$u_y-v_x=0 \tag{A.2}$$

which are a composite of the continuity equation and Euler's equation (A.1) and the *irrotational* condition eqn (A.2), the compatability equations are shown in [10] to be,

$$\left(\frac{dV}{V}\right)_{\pm}=\pm d\theta\tan\mu+\frac{\sin\mu\tan\mu\sin\theta}{\sin(\theta\pm\mu)}\left(\frac{dy}{y}\right)_{\pm}. \tag{A.3}$$

The equations are valid along the characteristic lines,

$$\left(\frac{dy}{dx}\right)_{\pm}=\tan(\theta\pm\mu) \tag{A.4}$$

Equations (A.3) are readily expressed in finite difference form and can therefore be easily integrated over a mesh of characteristic curves described by equations (A.3) and (A.4).

Four equations are available relating the five variables x, y, V, θ and μ, so one additional relationship is needed. This is found by using the definition of the Mach angle,

$$\mu = \sin^{-1}\left(\frac{1}{M}\right), \tag{A.5}$$

and a real-gas relationship between M and V. The latter is achieved by tabulating M and V through an isentropic expansion including real-gas effects. In general, the four equations are integrated in a marching scheme using the modified Euler predictor/corrector method with an iterative algorithm on the corrector step. Details of this procedure are found in [10]. A direct marching technique is used for the design and analysis procedures, meaning that the left and right running characteristic waves (C_+ and C_- characteristics, respectively) make-up the computational grid.

A.1 Design Procedure

The MOC design procedure used here is based primarily on that of reference [8], which is a modification of the work presented in [7]. Integration begins with the design condition. That is, the starting solution is the final characteristic DE in Fig. 1.3. For this approach one must specify the solution along ABDE. The maximum turning angle of a contoured nozzle occurs at point C of Fig. 1.3, the

inflection point. The angle of the characteristic wall here, θ_c, must be specified.

A.1.1 Radial Flow Region

Region II of Fig. 1.3 is called the radial flow region and is governed by the characteristic radial flow equations, (A.6) and (A.7), which are the Prandtl-Meyer expansion function and the radial velocity relationship.

$$\theta_I = \int_0^{\theta_f} d\theta_f = \frac{1}{2}\int_{V_{M=1}}^{V} \frac{(M^2-1)^{\frac{1}{2}}}{V} dV \tag{A.6}$$

and

$$ln\left(\frac{r}{r_{cr}}\right) = \frac{1}{2}\int_{V_{M=1}}^{V} \frac{(M^2-1)}{V} dV. \tag{A.7}$$

Here θ_f is the flow angle and θ_I is the Prandtl-Meyer expansion function for radial flow. For these equations, r is the distance from the source shown on the centerline upstream of point A in Fig. 1.3, and r_{cr} is the sonic radius in source flow. These equations are numerically integrated using an arbitrarily small velocity step ΔV and the tabulated relation for M and V until the known design velocity is reached. The integration of eq. (A.7) to V_D fixes the location of point D. The relationship between $\frac{r}{r_{cr}}$, V, θ_I is retained and used as the centerline solution on BD. Using the relations,

$$\theta_f = \theta_{I_D} - \theta_I \quad \text{along CD} \tag{A.8}$$

and

$$\theta_f = \theta_I - \theta_{I_B} \quad \text{along BC} \tag{A.9}$$

equation (A.10) is derived.

$$\theta_{I_B} = \theta_{I_D} - 2\theta_C. \tag{A.10}$$

θ_{I_B} can now be used in conjunction with the previously retained relationship between θ_I and $\frac{r}{r_{cr}}$ to determine the location and flow solution at point B. The centerline solution is now fixed on AB by assuming a M or V distribution. Using sonic conditions at A and the known solution at B, one has the freedom to specify a first, second or third order distribution. With the solution now fixed along ABD, it is left to determine the solution at the exit, the starting point of integration, line DE.

A.1.2 Uniform Flow Region

Region IV is the uniform flow region of a contoured nozzle since it is desired to have constant properties and no flow angularity. Therefore, the solution along DE is known to be the design conditions. However, it is still left to spacially locate point E, which is fixed by the mass flux through the nozzle since all flow properties on DE are known. The calculation of the limiting mass flux employs the stream function concept and is reviewed in the following section.

A.1.3 Stream Function and Inviscid Wall Boundary

Integration along the characteristics for the design procedure begins at the centerline where there are two points of known solution. A C_+ characteristic through a centerline point and a C_- characteristic through a point on the starting characteristic are used to simultaneously integrate equations (A.3) and (A.4) for the flow

solution at another point on the second right running characteristic. The general procedure is to calculate the stream function, ψ, along with the other flow variables, at each point until it reaches the value limited by the mass flow. ψ_{lim} is calculated in the radial flow region at point C, the inflection point of the contour. Integration of the axisymmetric radial flow relation for ψ, eq.(A.11),

$$d\overline{\psi} = \left(\frac{\rho}{\rho_t}\right) W \left(\frac{r}{r_{cr}}\right)^2 \sin\theta_f d\theta_f \tag{A.11}$$

where

$$\overline{\psi} = \frac{\psi}{\rho_t u_l r_{cr}^2}$$

gives the following result after evaluating a constant of integration.

$$\overline{\psi} = \left(\frac{\rho}{\rho_t}\right) W \left(\frac{r}{r_{cr}}\right)^2 (1 - \cos\theta_f). \tag{A.12}$$

Again, equations (A.8) and (A.9) are used with the retained radial flows relationship to determine $\frac{r}{r_{cr}}$ and V at point C. The real-gas relationship between ρ and V is obtained from tables. The equation for ψ used while integrating the characteristic mesh is

$$\overline{\psi} = \int_0^s \frac{\rho}{\rho_t} V \sin\mu \left(\frac{r}{r_{cr}^2}\right) ds. \tag{A.13}$$

where s refers to the distance along the Mach wave and y is the perpendicular distance from the x axis. When, during integration of eqs. (A.13), ψ_{lim} is reached, integration stops, the wall point location is recorded and a new Mach line is started.

A.1.4 Iterative Procedure

For the present designs the exit radius is a design constraint. This means that two nested iterative procedures will be needed to get a converged design. The outer iteration is set up to converge on the design exit radius. The inner iteration is designed to converge on the correct value of δ^* at each x station for each contour in the outer iteration.

An initial guess for δ^* at the exit is necessary and the nondimensional inviscid contour is scaled so that its exit radius is equal to the design radius minus the guessed δ^*. The boundary layer code (see Appendix B) is used to generate δ^* for these coordinates and this is added to the scaled inviscid coordinates to get an initial guess for the corrected wall, y_{corr}. Now, each time the coordinates are scaled or adjusted the curvilinear distance, s, of the nozzle contour is changed and since $\delta^* = \delta^*(s)$, the displacement thickness is also changed. So, a second iterative procedure is followed to find the correct value of δ^* at each x-location. Here y_{corr} is adjusted at each x-location by

$$\Delta_{wall} = \frac{1}{2}(y_{inv} - y_{corr} + \delta^*)$$

after every iteration on δ^* until Δ_{wall} is less than a specified small ϵ.

If the exit radius of the newly adjusted wall is not equal to the design radius, then this wall is scaled to the design exit radius and the inner iteration loop is repeated until they are equal.

A.2 Analysis Procedure

The present MOC analysis code is based on chapters 12 through 15 of [10]. Integration of eqs (A.3) and (A.4) along the characteristics proceeds as in the design case. The main differences between the design and analysis procedures are in the starting solution and the techniques for dealing with the boundaries. Integration begins near the throat on what is referred to as the initial value solution.

A.2.1 Wall Point

Sketch A.1 illustrates the wall point situation. The presence of the solid boundary clearly eliminates the C_- characteristic. However, the wall location is known and the flow tangency relationships, θ are known (the slope of the wall). So for the three unknowns, M, μ and V we have three equations, the compatability equation for the C_+ characteristic, the tabular real-gas isentropic expansion of the gas and the Mach wave relation.

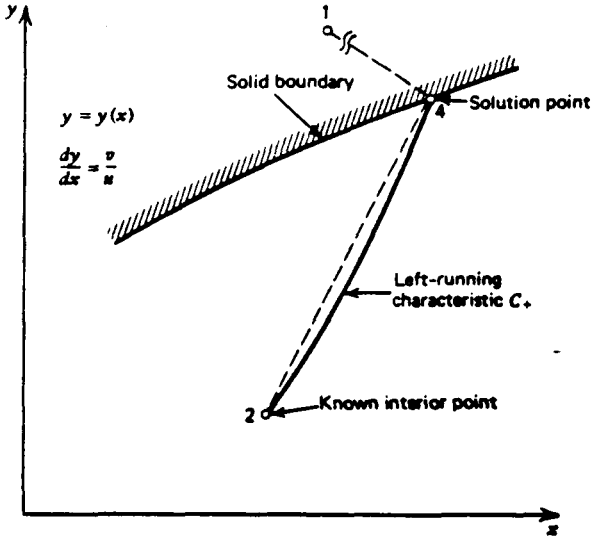

Sketch A.1 Direct wall point solution by MOC.

$$\left(\frac{dV}{V}\right) = d\theta \tan\mu + \frac{\sin\mu\tan\mu\sin\theta}{\sin(\theta+\mu)}\left(\frac{dy}{y}\right),$$

$$\mu = \sin^{-1}\left(\frac{1}{M}\right),$$

$$\frac{dy}{dx} = \tan\theta = \frac{v}{u},$$

$$M = M(V).$$

A.2.2 Centerline Point

A similar situation arises at the axis (see sketch A.2). However for this case both characteristics exist. The flow properties at point 1 are merely reflected to point 2 exploiting the symmetry condition of the axisymmetric centerline. Furthermore, compatability equations are simplified greatly since y or v are zero at the centerline

so that only the C_- characteristic is needed.

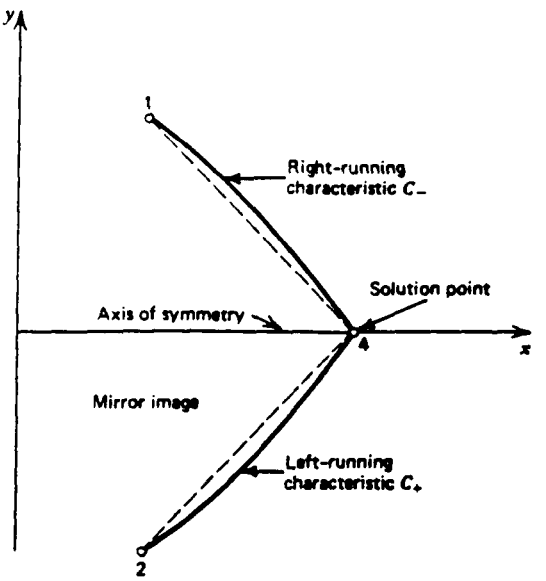

Sketch A.2 Centerline point solution by MOC.

A.2.3 Iterative Procedure

To start the analysis iteration, an initial guess for δ^* is needed. This is obtained by generating a boundary layer using one-dimensional isentropic expansion to the design Mach number as the edge conditions. The boundary layer correction is subtracted from the actual nozzle wall to get a first guess for the characteristic coordinates. The MOC analysis code is run on these coordinates. From the analysis output, a second, hopefully better, estimate of δ^* is generated. This is iterated until the changes in δ^* are small.

When and if a strong oblique shock wave forms in the MOC analysis solution, then convergence may not be reached. The current status of the MOC/BL anal-

ysis procedure is not generally sophisticated enough to account for strong shock-wave/boundary layer interactions.

2 Numerical Solution of the Boundary Layer Equations

E. C. Anderson developed a computer program with the objective of generating turbulent boundary layer solutions for hypersonic flows, external and internal [9]. A brief overview of the techniques used is presented here.

The Crank-Nicolson semi-implicit finite difference method is employed to integrate the steady momentum, energy, species, and continuity equations. The program is limited to gases in chemical equilibrium. By assuming a constant gas composition across the boundary layer, the effects of chemical reactions are included in the heat transfer terms of the energy equation. In terms of non-dimensional variables these equations are, in axisymmetric form,

Continuity

$$\frac{(\partial \rho u r)}{\partial x} + \frac{\partial[(\rho v + \overline{\rho' v'})r]}{\partial y} = 0 \tag{2.1}$$

Momentum

$$\rho u \frac{\partial u}{\partial x} + (\rho v + \overline{\rho' v'}) \frac{\partial u}{\partial y} = \rho_e u_e \frac{du_e}{dx} + \frac{\partial}{\partial y}\left(\mu \frac{\partial u}{\partial y} - \rho \overline{u' v'}\right) \tag{2.2}$$

Energy

$$\rho u \frac{\partial H}{\partial x} + (\rho v + \overline{\rho' v'}) \frac{\partial H}{\partial y} = \frac{\partial}{\partial y}\left[\frac{\mu}{Pr} \frac{\partial H}{\partial y} - \rho \overline{v' H'} + \mu \left(1 - \frac{1}{Pr}\right) u \frac{\partial u}{\partial y}\right] \tag{2.3}$$

The above non-dimensional, turbulent boundary layer equations are transformed using the Levy-Lees transformation (eqs. B.4 and B.5) to appear in the form of equations (B.6), (B.7) and (B.8).

$$\xi(x) = \int_0^x \rho_e u_e \mu_e r^2 dx \tag{2.4}$$

$$\eta(x,y) = \frac{\rho_e u_e r}{(2\xi)^{\frac{1}{2}}} \frac{du_e}{dx} \int_0^y \frac{\rho}{\rho_e} dy \tag{2.5}$$

Continuity

$$2\xi F_\xi + V' + F = 0 \tag{2.6}$$

Momentum

$$2\xi F F_\xi + V F_\eta = \beta\left(\frac{\rho_e}{\rho} - F^2\right) + (C(1+\epsilon^+)F')' \tag{2.7}$$

Energy

$$\begin{aligned} 2\xi F g_\xi + V g' = {} & \frac{C}{Pr}\left(1+\epsilon^+\frac{Pr}{Pr_t}\right)g'' + \left[\frac{C}{Pr}\left(1+\epsilon^+\frac{Pr}{Pr_t}\right)\right]' g' \\ & + \frac{u_e^2}{H_e}\{C_1\left[C'FF' + C(F'^2 + F'')\right] + CFF'C_1'\} \end{aligned} \tag{2.8}$$

where,

$$V = \frac{2\xi}{\rho_e u_e \mu_e r^2}\left[f'\eta_x + \frac{(\rho v + \overline{\rho' v'})r}{(2\xi)^{\frac{1}{2}}}\right]$$

$$F = f' = \frac{u}{u_e}; \quad g = \frac{H}{H_e}; \quad C = \frac{\rho\mu}{\rho_e u_e}$$

$$\beta = \frac{2\xi}{u_e}\frac{du_e}{d\xi}$$

Since Crank-Nicolson technique is semi-implicit, the finite difference representation of these equations contains independent variables at the station where the solution is desired. This requires a matrix inversion, or an iterative procedure. An

iterative procedure is used here. The coefficients of the independent variables are evaluated using properties at the previous station. The finite difference equations for energy and momentum are solved for the independent variables at the new station. At each iteration the continuity equation is integrated using the trapezoidal rule for the normal velocity, v. From the new properties, better estimates for the coefficients are calculated and the procedure is iterated until converged.

Once the solution has converged at a particular station, eq (B.9) is integrated trapezoidally from the wall to the point where $\rho u/\rho_e U_e = 0.995$.

$$\delta^* = \int_0^{y_e} \left(1 - \frac{\rho u}{\rho_e U_e}\right)(r_o - y\cos\theta)\,dy - \frac{\Delta w_e}{\rho_e U_e} \tag{2.9}$$

The point in the boundary layer where this occurs is called the displacement thickness and is used as the boundary layer correction to the MOC inviscid flow region.

The turbulence model is algebraic and is based on a two layer eddy viscosity assumption. Hence, the Reynolds stress and turbulent heat transfer are defined as follows.

$$-\rho\overline{u'v'} = \varepsilon^+ \frac{\partial u}{\partial y} \tag{2.10}$$

$$-\rho\overline{v'H'} = \frac{C_p \varepsilon_h}{Pr_t}\frac{\partial H}{\partial y} \tag{2.11}$$

where,

$$Pr_t = \frac{C_p \varepsilon^+}{\varepsilon_h}$$

The total shear stress and heat transfer become,

$$\tau = \left(\mu + \varepsilon^+\right)\frac{\partial u}{\partial y} \tag{2.12}$$

and,

$$q = \left(k + \frac{C_p \varepsilon^+}{Pr_t}\right) \frac{\partial H}{\partial y} \tag{2.13}$$

The eddy viscosity is modeled assuming two layers. Both inner layer and outer layer models for ε^+ are evaluated until

$$\varepsilon_i^+ = \varepsilon_o^+.$$

Below this point in the boundary layer ε_i^+ is used and above this point ε_o^+ is used.

The outer layer is modeled by a zero equation model developed by Clauser (eq. B.14).

$$\varepsilon_o^+ = k_2 \frac{\rho u_e}{\mu \epsilon_{VD}^2} \frac{\delta_k}{a} \gamma \tag{2.14}$$

Here, δ_k is the incompressible displacement thickness, ϵ_{VD} is a coordinate stretching parameter, and k_2 is an empirical constant.

The inner layer is based on Prandtl's mixing length theory and uses the Cebeci-Smith zero equation turbulence model. The eddy viscosity for this layer is,

$$\varepsilon_i^+ = x_1 \left\{1 - exp\left[-x_2 \left(\left|\frac{\hat{C}_{f_\infty}}{2} - \frac{y}{\rho} \rho_e u_e \frac{du_e}{dx}\right|\right)^{\frac{1}{2}}\right]\right\} |F'| \tag{2.15}$$

where,

$$x_1 = \frac{(k_1 y \rho u_e)^2 r}{\epsilon_{VD} \mu (2\xi)^{\frac{1}{2}}}$$

$$x_2 = \frac{y\rho}{26 \mu \epsilon_{VD}^{\frac{1}{2}}}$$

$$k_1 = \text{constant.}$$

3 Turbulence Modeling for Navier-Stokes Solutions

The turbulent Navier-Stokes equations are identical to the laminar equations with the exception of additional terms in the turbulent expressions for heat transfer (3.1) and the stress tensor (3.2).

$$q_i = -k\frac{\partial T}{\partial x_i} + \rho C_p \overline{u_i' T'} \tag{3.1}$$

$$\tau_{ij} = \mu\left[\left(\frac{\partial u_i}{\partial x_j} + \frac{\partial u_j}{\partial x_i}\right) - \frac{2}{3}\delta_{ij}\frac{\partial u_m}{\partial x_m}\right] - \rho\overline{u_i' u_j'} \tag{3.2}$$

However, these two terms introduce many additional unknowns to the problem which can be defined only by the already unknown turbulent structure. These unknowns are dependant not only upon the physical properties of the particular gas, but also upon local conditions such as velocity, geometry, surface roughness, and previous spacial and temporal conditions [13]. Following the original idea of Boussinesq (1877), one can model the *effect* of turbulence — rather than model the actual physics — and approach mathematical closure by considering the turbulent terms as functions of local geometry and flow properties. By defining the turbulent shear (3.3) and turbulent heat transfer (3.4) in terms of effective turbulent coefficients of viscosity, μ_t and thermal conductivity, k_t,

$$-\rho\overline{u_i' u_j'} = \mu_t\left[\left(\frac{\partial u_i}{\partial x_j} + \frac{\partial u_j}{\partial x_i}\right) - \frac{2}{3}\delta_{ij}\frac{\partial u_m}{\partial x_m}\right] \tag{3.3}$$

$$-kC_p\overline{u_i' T'} = k_t\frac{\partial T}{\partial x_i} \tag{3.4}$$

the assumption is that the turbulent terms behave similarly to their laminar (i.e. , physical) counterparts. Thus, in the stress and heat transfer equations of equation set (2.1),

$$\mu = \mu_l + \mu_t$$

and

$$k = k_l + k_t$$

In this research the turbulent conductivity is supplied through the turbulent Prandtl number,

$$Pr_t = \frac{C_p \mu_t}{k_t}$$

and is considered to be constant at an empirical value of 0.9. The turbulent viscosity is furnished by the Baldwin-Lomax two layer eddy viscosity model [14].

3.1 Baldwin-Lomax Turbulence Model

The Baldwin-Lomax two layer eddy viscosity model was developed to address the problem of including turbulent effects in Navier-Stokes simulations of separated flows where the boundary layer thickness is not generally known. Baldwin and Lomax [14] defined the eddy viscosity on an inner and outer layer by

$$\mu_t = \begin{cases} (\mu_t)_{inner} & y \leq y_{crossover} \\ (\mu_t)_{outer} & y > y_{crossover} \end{cases} \tag{3.5}$$

where $y_{crossover}$ is the shortest normal distance from the wall at which the inner and outer coefficients are equal.

The Prandtl-Van Driest formulation is used for the inner region.

$$(\mu_t)_{inner} = \rho l^2 |\omega| \tag{3.6}$$

where

$$l = ky\left[1 - \exp\left(-y^+/A^+\right)\right] \tag{3.7}$$

$|\omega|$ is the magnitude of the vorticity

$$|\omega| = \frac{\partial u}{\partial y} - \frac{\partial v}{\partial x} \tag{3.8}$$

and

$$y^+ = \frac{\sqrt{\rho_w \tau_w}\, y}{\mu_w} \tag{3.9}$$

The formulation for the outer region is

$$(\mu_t)_{outer} = K C_{CP} \rho F_{wake} F_{Kleb}(y) \tag{3.10}$$

where K is the Clauser constant C_{CP} is an additional constant and

$$F_{wake} = \left\{ \begin{array}{c} y_{max} F_{max} \\ C_{wk} y_{max} u_{dif}^2 / F_{max} \end{array} \right\}_{min} \tag{3.11}$$

The maximum point of the function (3.12) and the point at which it occurs define F_{max} and y_{max}.

$$F(y) = y\,|\omega|\left[1 - \exp\left(-y^+/A^+\right)\right] \tag{3.12}$$

F_{Kleb} is the Klebanoff intermittency factor expressed as

$$F_{Kleb}(y) = \left[1 + 5.5\left(\frac{C_{Kleb}\, y}{y_{max}}\right)^6\right]^{-1} \tag{3.13}$$

and the quantity u_{dif} is the difference between the maximum and minimum total velocities, which for no slip boundary conditions is the maximum total velocity in the profile. The following constants are used in the turbulent viscosity calculations.

$$A^+ = 26$$

$$C_{CP} = 1.6$$

$$C_{Klob} = 0.3$$

$$C_{wk} = 0.25$$

$$k = 0.4$$

$$K = 0.0168$$

Tables

Table 1. Design Conditions and Constraints

Nozzle	Working Gas	Exit Diam.	Exit Mach	Total Length	P_o psia	T_o °R
$N_2 - 17$	Nitrogen	20 in.	17	—	4000	3400
$N_2 - 13$	Nitrogen	20 in.	13.5	—	4000	3000
CF_4	CF_4	20 in.	5.95	—	1600	1260
He-20	Helium	21 in.	20	124 in.	1500	600
Air	Air	~ 7.2 in.	5.95	~ 76 in.	45	1260

Table 2. Constants for CF_4 Thermodynamic Equations

R	94.47002	b	0.0015
A_2	-58.11999	A_3	7.387702×10^{-3}
B_2	0.1032692	B_3	3.873415×10^{-5}
C_2	-508.9595	C_3	0.9054616
A_4	2.011774×10^{-5}	A_5	-2.929506×10^{-8}
B_4	-7.385870×10^{-8}	B_5	1.066416×10^{-10}
A_6	4.025724×10^{11}	C_5	-3.162000×10^{-7}
B_6	-1.149705×10^{9}	K	1.758236
α	-1.059139×10^{4}	-	

C onstants for Enthalpy and Entropy Equations

for temperature interval 100 K to 615 K,

a_4	1.43308×10^{2}	b_4	1.51168
c_4	5.15767×10^{-4}	d_4	-1.59381×10^{-6}

for temperature interval 615 K to 1500 K.

a_4	2.95790×10^{2}	b_4	1.53754
c_4	-1.0727×10^{-3}	d_4	2.64172×10^{-7}

Table 3. Design Wall Coordinates for the Air Nozzle

x, in.	r, in.
0.0000	0.9015
0.1000	0.9033
0.2000	0.9051
0.3000	0.9077
0.4000	0.9111
0.5000	0.9152
0.6000	0.9200
0.7000	0.9254
0.8000	0.9315
0.9000	0.9382
1.0000	0.9454
1.1000	0.9533
1.2000	0.9618
1.3000	0.9708
1.4000	0.9804
1.5000	0.9906
1.6000	1.0013
1.7000	1.0126
1.8000	1.0245
1.9000	1.0369
2.0000	1.0499
2.1000	1.0635
2.2000	1.0776
2.3000	1.0923
2.4000	1.1075
2.5000	1.1231
2.6000	1.1392
2.7000	1.1558
2.8000	1.1727
2.9000	1.1900
3.0000	1.2076
3.1000	1.2255
3.2000	1.2438
3.3000	1.2623
3.4000	1.2810
3.5000	1.3001
3.6000	1.3193
3.7000	1.3387
3.8000	1.3583
3.9000	1.3781
4.0000	1.3981
4.1000	1.4182
4.2000	1.4385
4.3000	1.4589
4.4000	1.4795
4.5000	1.5001
4.6000	1.5209
4.7000	1.5418
4.8000	1.5627
4.9000	1.5838
5.0000	1.6049
5.1000	1.6262
5.2000	1.6474

x, in.	r, in.
5.3000	1.6688
5.4000	1.6903
5.5000	1.7117
5.6000	1.7333
5.7000	1.7549
5.8000	1.7765
5.9000	1.7982
6.0000	1.8200
6.1000	1.8417
6.2000	1.8636
6.3000	1.8854
6.4000	1.9073
6.5000	1.9292
6.6000	1.9511
6.7000	1.9731
6.8000	1.9951
6.9000	2.0171
7.0000	2.0392
7.1000	2.0613
7.2000	2.0833
7.3000	2.1055
7.4000	2.1276
7.5000	2.1497
7.6000	2.1719
7.7000	2.1941
7.8000	2.2162
7.9000	2.2385
8.0000	2.2607
8.2000	2.3051
8.4000	2.3496
8.6000	2.3942
8.8000	2.4388
9.0000	2.4834
9.2000	2.5281
9.4000	2.5727
9.6000	2.6170
9.8000	2.6611
10.0000	2.7049
10.2000	2.7484
10.4000	2.7916
10.6000	2.8345
10.8000	2.8771
11.0000	2.9193
11.2000	2.9611
11.4000	3.0027
11.6000	3.0439
11.8000	3.0848
12.0000	3.1253
12.2000	3.1655
12.4000	3.2054
12.6000	3.2449
12.8000	3.2840
13.0000	3.3229

Table 3. (continued)

x, in.	r, in.
13.2000	3.3614
13.4000	3.3996
13.6000	3.4375
13.8000	3.4750
14.0000	3.5122
14.2000	3.5491
14.4000	3.5857
14.6000	3.6219
14.8000	3.6579
15.0000	3.6935
15.2000	3.7288
15.4000	3.7638
15.6000	3.7985
15.8000	3.8330
16.0000	3.8671
16.2000	3.9009
16.4000	3.9345
16.6000	3.9677
16.8000	4.0007
17.0000	4.0333
17.2000	4.0657
17.4000	4.0978
17.6000	4.1297
17.8000	4.1612
18.0000	4.1925
18.2000	4.2235
18.4000	4.2543
18.6000	4.2847
18.8000	4.3150
19.0000	4.3449
19.2000	4.3746
19.4000	4.4040
19.6000	4.4332
19.8000	4.4622
20.0000	4.4909
20.2000	4.5193
20.4000	4.5475
20.6000	4.5755
20.8000	4.6032
21.0000	4.6307
21.2000	4.6580
21.4000	4.6850
21.6000	4.7118
21.8000	4.7383
22.0000	4.7646
22.2000	4.7907
22.4000	4.8166
22.6000	4.8422
22.8000	4.8677
23.0000	4.8929
23.5000	4.9549
24.0000	5.0157
24.5000	5.0752
25.0000	5.1334
25.5000	5.1904
26.0000	5.2461
26.5000	5.3007
27.0000	5.3541
27.5000	5.4063

x, in.	r, in.
28.0000	5.4574
28.5000	5.5075
29.0000	5.5564
29.5000	5.6043
30.0000	5.6511
30.5000	5.6970
31.0000	5.7418
31.5000	5.7857
32.0000	5.8285
32.5000	5.8705
33.0000	5.9115
33.5000	5.9516
34.0000	5.9908
34.5000	6.0292
35.0000	6.0666
35.5000	6.1033
36.0000	6.1391
36.5000	6.1740
37.0000	6.2082
37.5000	6.2416
38.0000	6.2742
38.5000	6.3060
39.0000	6.3371
39.5000	6.3674
40.0000	6.3971
40.5000	6.4260
41.0000	6.4542
41.5000	6.4817
42.0000	6.5085
42.5000	6.5347
43.0000	6.5602
43.5000	6.5851
44.0000	6.6094
44.5000	6.6330
45.0000	6.6560
45.5000	6.6784
46.0000	6.7002
46.5000	6.7215
47.0000	6.7421
47.5000	6.7622
48.0000	6.7818
48.5000	6.8008
49.0000	6.8193
49.5000	6.8372
50.0000	6.8547
51.0000	6.8880
52.0000	6.9194
53.0000	6.9489
54.0000	6.9766
55.0000	7.0026
56.0000	7.0268
57.0000	7.0494
58.0000	7.0705
59.0000	7.0901
60.0000	7.1082
61.0000	7.1249
62.0000	7.1403
63.0000	7.1544
64.0000	7.1672

Table 3. (continued)

x, in.	r, in.
65.0000	7.1789
66.0000	7.1891
67.0000	7.1976
68.0000	7.2057
69.0000	7.2137
70.0000	7.2217

x, in.	r, in.
71.0000	7.2296
72.0000	7.2374
73.0000	7.2451
74.0000	7.2528
75.0000	7.2605
76.0000	7.2681

Table 4. Design Wall Coordinates for the N_2 – 13.5 Nozzle

x, in.	r, in.
0.0000	0.1194
0.1000	0.1202
0.2000	0.1224
0.3000	0.1256
0.4000	0.1298
0.5000	0.1351
0.6000	0.1413
0.7000	0.1484
0.8000	0.1566
0.9000	0.1657
1.0000	0.1757
1.1000	0.1869
1.2000	0.1990
1.3000	0.2122
1.4000	0.2266
1.5000	0.2421
1.6000	0.2587
1.7000	0.2762
1.8000	0.2946
1.9000	0.3135
2.0000	0.3331
2.1000	0.3531
2.2000	0.3735
2.3000	0.3943
2.4000	0.4153
2.5000	0.4365
2.6000	0.4579
2.7000	0.4796
2.8000	0.5013
2.9000	0.5232
3.0000	0.5452
3.1000	0.5673
3.2000	0.5895
3.3000	0.6117
3.4000	0.6341
3.5000	0.6564
3.6000	0.6789
3.7000	0.7014
3.8000	0.7239
3.9000	0.7465
4.0000	0.7692
4.1000	0.7918
4.2000	0.8146
4.3000	0.8373
4.4000	0.8601
4.5000	0.8829
4.6000	0.9058
4.7000	0.9287
4.8000	0.9516
4.9000	0.9745
5.0000	0.9974
5.1000	1.0204
5.2000	1.0433

x, in.	r, in.
5.3000	1.0661
5.4000	1.0888
5.5000	1.1114
5.6000	1.1339
5.7000	1.1563
5.8000	1.1785
5.9000	1.2007
6.0000	1.2228
6.1000	1.2447
6.2000	1.2666
6.3000	1.2883
6.4000	1.3099
6.5000	1.3315
6.6000	1.3529
6.7000	1.3742
6.8000	1.3954
6.9000	1.4165
7.0000	1.4375
7.1000	1.4584
7.2000	1.4792
7.3000	1.4999
7.4000	1.5205
7.5000	1.5410
7.6000	1.5614
7.7000	1.5817
7.8000	1.6019
7.9000	1.6220
8.0000	1.6420
8.1000	1.6619
8.2000	1.6818
8.3000	1.7015
8.4000	1.7211
8.5000	1.7406
8.6000	1.7601
8.7000	1.7794
8.8000	1.7987
8.9000	1.8179
9.0000	1.8370
9.1000	1.8560
9.2000	1.8749
9.3000	1.8937
9.4000	1.9125
9.5000	1.9311
9.6000	1.9497
9.7000	1.9682
9.8000	1.9867
9.9000	2.0050
10.0000	2.0233
10.1000	2.0414
10.2000	2.0595
10.3000	2.0776
10.4000	2.0955
10.5000	2.1134

Table 4. (continued)

x, in.	r, in.
10.6000	2.1312
10.7000	2.1489
10.8000	2.1666
10.9000	2.1841
11.0000	2.2017
11.1000	2.2191
11.2000	2.2365
11.3000	2.2538
11.4000	2.2710
11.5000	2.2882
11.6000	2.3052
11.7000	2.3223
11.8000	2.3392
11.9000	2.3561
12.0000	2.3730
12.2000	2.4064
12.4000	2.4397
12.6000	2.4727
12.8000	2.5054
13.0000	2.5379
13.2000	2.5702
13.4000	2.6023
13.6000	2.6341
13.8000	2.6657
14.0000	2.6971
14.2000	2.7282
14.4000	2.7592
14.6000	2.7899
14.8000	2.8204
15.0000	2.8508
15.2000	2.8809
15.4000	2.9109
15.6000	2.9406
15.8000	2.9702
16.0000	2.9996
16.2000	3.0287
16.4000	3.0577
16.6000	3.0866
16.8000	3.1152
17.0000	3.1437
17.2000	3.1720
17.4000	3.2001
17.6000	3.2281
17.8000	3.2559
18.0000	3.2835
18.2000	3.3110
18.4000	3.3383
18.6000	3.3654
18.8000	3.3925
19.0000	3.4193
19.2000	3.4460
19.4000	3.4725
19.6000	3.4989
19.8000	3.5251
20.0000	3.5512
20.3000	3.5901
20.6000	3.6286
20.9000	3.6668
21.2000	3.7047

x, in.	r, in.
21.5000	3.7423
21.8000	3.7796
22.1000	3.8166
22.4000	3.8533
22.7000	3.8898
23.0000	3.9259
23.3000	3.9618
23.6000	3.9974
23.9000	4.0327
24.2000	4.0678
24.5000	4.1026
24.8000	4.1371
25.1000	4.1714
25.4000	4.2054
25.7000	4.2392
26.0000	4.2728
26.3000	4.3061
26.6000	4.3391
26.9000	4.3720
27.2000	4.4046
27.5000	4.4369
27.8000	4.4691
28.1000	4.5010
28.4000	4.5327
28.7000	4.5642
29.0000	4.5954
29.3000	4.6265
29.6000	4.6574
29.9000	4.6880
30.2000	4.7184
30.5000	4.7487
30.8000	4.7787
31.1000	4.8085
31.4000	4.8382
31.7000	4.8676
32.0000	4.8969
32.3000	4.9259
32.6000	4.9548
32.9000	4.9835
33.2000	5.0120
33.5000	5.0403
33.8000	5.0685
34.1000	5.0964
34.4000	5.1242
34.7000	5.1519
35.0000	5.1793
35.3000	5.2066
35.6000	5.2337
35.9000	5.2607
36.2000	5.2875
36.5000	5.3141
36.8000	5.3405
37.1000	5.3668
37.4000	5.3930
37.7000	5.4189
38.0000	5.4448
38.3000	5.4704
38.6000	5.4960
38.9000	5.5213

Table 4. (continued)

x, in.	r, in.
39.2000	5.5465
39.5000	5.5716
39.8000	5.5965
40.1000	5.6213
40.4000	5.6459
40.7000	5.6704
41.0000	5.6947
41.3000	5.7189
41.6000	5.7430
41.9000	5.7669
42.2000	5.7907
42.5000	5.8144
42.8000	5.8379
43.1000	5.8613
43.4000	5.8845
43.7000	5.9076
44.0000	5.9306
44.3000	5.9535
44.6000	5.9762
44.9000	5.9988
45.2000	6.0212
45.5000	6.0436
45.8000	6.0658
46.1000	6.0879
46.4000	6.1099
46.7000	6.1317
47.0000	6.1535
47.3000	6.1751
47.6000	6.1966
47.9000	6.2180
48.2000	6.2392
48.5000	6.2604
48.8000	6.2814
49.1000	6.3023
49.4000	6.3231
49.7000	6.3438
50.0000	6.3644
50.5000	6.3984
51.0000	6.4321
51.5000	6.4655
52.0000	6.4987
52.5000	6.5315
53.0000	6.5641
53.5000	6.5963
54.0000	6.6283
54.5000	6.6600
55.0000	6.6914
55.5000	6.7225
56.0000	6.7533
56.5000	6.7839
57.0000	6.8143
57.5000	6.8443
58.0000	6.8741
58.5000	6.9036
59.0000	6.9329
59.5000	6.9619
60.0000	6.9907
60.5000	7.0192
61.0000	7.0475

x, in.	r, in.
61.5000	7.0755
62.0000	7.1032
63.0000	7.1581
64.0000	7.2119
65.0000	7.2649
66.0000	7.3169
67.0000	7.3681
68.0000	7.4183
69.0000	7.4677
70.0000	7.5163
71.0000	7.5640
72.0000	7.6108
73.0000	7.6569
74.0000	7.7021
75.0000	7.7465
76.0000	7.7902
77.0000	7.8330
78.0000	7.8752
79.0000	7.9165
80.0000	7.9571
81.0000	7.9970
82.0000	8.0362
83.0000	8.0747
84.0000	8.1124
85.0000	8.1495
86.0000	8.1858
87.0000	8.2215
88.0000	8.2565
89.0000	8.2908
90.0000	8.3245
91.0000	8.3575
92.0000	8.3899
93.0000	8.4216
94.0000	8.4526
95.0000	8.4830
96.0000	8.5128
97.0000	8.5419
98.0000	8.5704
99.0000	8.5983
100.0000	8.6256
101.0000	8.6523
102.0000	8.6783
103.0000	8.7037
104.0000	8.7286
105.0000	8.7528
106.0000	8.7764
107.0000	8.7993
108.0000	8.8217
109.0000	8.8435
110.0000	8.8646
111.0000	8.8850
112.0000	8.9049
113.0000	8.9240
114.0000	8.9424
115.0000	8.9601
116.0000	8.9768
117.0000	8.9924
117.5410	9.0000

Table 5. Design Wall Coordinates for the $N_2 - 17$ Nozzle

x, in.	r, in.
0.0000	0.0607
0.0018	0.0607
0.0066	0.0607
0.0135	0.0607
0.0235	0.0607
0.0379	0.0608
0.0585	0.0608
0.0883	0.0609
0.1311	0.0610
0.1928	0.0611
0.2817	0.0613
0.4096	0.0615
0.5934	0.0620
0.7934	0.0629
0.9934	0.0646
1.1934	0.0673
1.3934	0.0718
1.5934	0.0783
1.7934	0.0866
1.9934	0.0989
2.1934	0.1154
2.3934	0.1371
2.5934	0.1666
2.7934	0.2031
2.9934	0.2429
3.1934	0.2853
3.3934	0.3295
3.5934	0.3745
3.7934	0.4208
3.9934	0.4666
4.1934	0.5133
4.3934	0.5603
4.5934	0.6077
4.7934	0.6552
4.9934	0.7028
5.1934	0.7501
5.3934	0.7969
5.5934	0.8429
5.7934	0.8883
5.9934	0.9331
6.1934	0.9773
6.3934	1.0211
6.5934	1.0643
6.7934	1.1070
6.9934	1.1493
7.1934	1.1912
7.3934	1.2329
7.5934	1.2741
7.7934	1.3145
7.9934	1.3544
8.2134	1.3978
8.5302	1.4592

x, in.	r, in.
8.9302	1.5355
9.3302	1.6102
9.7302	1.6836
10.1302	1.7555
10.5302	1.8266
10.9302	1.8960
11.3302	1.9645
11.7302	2.0322
12.1302	2.0983
12.5302	2.1637
12.9302	2.2286
13.3302	2.2926
13.7302	2.3547
14.1302	2.4160
14.5302	2.4791
14.9302	2.5407
15.3302	2.6006
15.7302	2.6599
16.1302	2.7189
16.5302	2.7773
16.9302	2.8346
17.3302	2.8912
17.7302	2.9473
18.1302	3.0027
18.5302	3.0576
18.9302	3.1118
19.3302	3.1655
19.7302	3.2188
20.1302	3.2715
20.6582	3.3403
21.2582	3.4175
21.8582	3.4936
22.4582	3.5686
23.0582	3.6426
23.6582	3.7155
24.2582	3.7874
24.8582	3.8585
25.4582	3.9286
26.0582	3.9980
26.6582	4.0665
27.2582	4.1341
27.8582	4.2010
28.4582	4.2671
29.0582	4.3325
29.6582	4.3971
30.2582	4.4611
30.8582	4.5243
31.4582	4.5868
32.0582	4.6488
32.6582	4.7099
33.2582	4.7706
33.8582	4.8307

Table 5. (continued)

x, in.	r, in.
34.4582	4.8900
35.0582	4.9488
35.6582	5.0069
36.2582	5.0646
36.8582	5.1217
37.4582	5.1781
38.0582	5.2341
38.6582	5.2895
39.2582	5.3444
39.8582	5.3987
40.4582	5.4526
41.0582	5.5059
41.6582	5.5586
42.2582	5.6108
42.8582	5.6626
43.4582	5.7141
44.0582	5.7649
44.6582	5.8152
45.2582	5.8650
45.8582	5.9144
46.4582	5.9633
47.0582	6.0120
47.6582	6.0599
48.2582	6.1076
48.8582	6.1556
49.4582	6.2026
50.0582	6.2495
50.8182	6.3080
51.6182	6.3689
52.4182	6.4292
53.2182	6.4890
54.0182	6.5480
54.8182	6.6069
55.6182	6.6641
56.4182	6.7210
57.2182	6.7775
58.0182	6.8331
58.8182	6.8884
59.6182	6.9430
60.4182	6.9969
61.2182	7.0504
62.0182	7.1032
62.8182	7.1556
63.6182	7.2072
64.4182	7.2584
65.2182	7.3090
66.0182	7.3591
66.8182	7.4086
67.6182	7.4576
68.4182	7.5061
69.2182	7.5541
70.0182	7.6016
70.8182	7.6486
71.6182	7.6952
72.4182	7.7413
73.2182	7.7867
74.0182	7.8318
74.8182	7.8756

x, in.	r, in.
75.6182	7.9191
76.4182	7.9622
77.2182	8.0050
78.0182	8.0474
78.8182	8.0894
79.6182	8.1311
80.4182	8.1724
81.2182	8.2134
82.0182	8.2540
82.8182	8.2942
83.6182	8.3341
84.4182	8.3736
85.2182	8.4128
86.0182	8.4515
86.8182	8.4900
87.6182	8.5281
88.4182	8.5658
89.2182	8.6032
90.0182	8.6402
90.8182	8.6768
91.6182	8.7131
92.4182	8.7490
93.2182	8.7846
94.0182	8.8198
94.8182	8.8546
95.6182	8.8891
96.4182	8.9233
97.2182	8.9570
98.0182	8.9904
98.8182	9.0235
99.6182	9.0562
100.4180	9.0885
101.2180	9.1205
102.0180	9.1521
102.8180	9.1833
103.6180	9.2142
104.4180	9.2447
105.2180	9.2749
106.0180	9.3047
106.8180	9.3342
107.6180	9.3633
108.4180	9.3920
109.2180	9.4204
110.0180	9.4484
110.8180	9.4760
111.6180	9.5033
112.4180	9.5303
113.2180	9.5568
114.0180	9.5831
114.8180	9.6089
115.6180	9.6344
116.4180	9.6595
117.2180	9.6843
118.0180	9.7087
118.8180	9.7328
119.6180	9.7565
120.4180	9.7799
121.2180	9.8028

Table 5. (continued)

x, in.	r, in.
122.0180	9.8254
122.8180	9.8477
123.6180	9.8696
124.4180	9.8912
125.2180	9.9123

x, in.	r, in.
126.0180	9.9332
126.8180	9.9536
127.6180	9.9737
128.4180	9.9935
128.9060	10.0053

Table 6. Design Wall Coordinates for the CF_4 Nozzle

x, in.	r, in.
0.0000	0.2580
0.1000	0.2581
0.2000	0.2583
0.3000	0.2587
0.4000	0.2592
0.5000	0.2599
0.6000	0.2607
0.7000	0.2615
0.8000	0.2625
0.9000	0.2636
1.0000	0.2649
1.1000	0.2662
1.2000	0.2677
1.3000	0.2693
1.4000	0.2709
1.5000	0.2727
1.6000	0.2746
1.7000	0.2767
1.8000	0.2788
1.9000	0.2810
2.0000	0.2833
2.1000	0.2857
2.2000	0.2882
2.3000	0.2908
2.4000	0.2935
2.5000	0.2964

x, in.	r, in.
2.6000	0.2993
2.7000	0.3024
2.8000	0.3055
2.9000	0.3089
3.0000	0.3123
3.1000	0.3159
3.2000	0.3196
3.3000	0.3235
3.4000	0.3275
3.5000	0.3317
3.6000	0.3360
3.7000	0.3406
3.8000	0.3453
3.9000	0.3502
4.0000	0.3551
4.1000	0.3603
4.2000	0.3656
4.3000	0.3710
4.4000	0.3767
4.5000	0.3825
4.6000	0.3885
4.7000	0.3947
4.8000	0.4011
4.9000	0.4077
5.0000	0.4145
5.1000	0.4216

Table 6. (continued)

x, in.	r, in.
5.2000	0.4288
5.3000	0.4362
5.4000	0.4439
5.5000	0.4519
5.6000	0.4600
5.7000	0.4684
5.8000	0.4771
5.9000	0.4861
6.0000	0.4953
6.1000	0.5048
6.2000	0.5146
6.3000	0.5247
6.4000	0.5352
6.5000	0.5459
6.6000	0.5570
6.7000	0.5685
6.8000	0.5803
6.9000	0.5925
7.0000	0.6051
7.1000	0.6181
7.2000	0.6316
7.3000	0.6455
7.4000	0.6599
7.5000	0.6749
7.6000	0.6903
7.7000	0.7063
7.8000	0.7228
7.9000	0.7398
8.0000	0.7573
8.1000	0.7752
8.2000	0.7936
8.3000	0.8124
8.4000	0.8316
8.5000	0.8511
8.6000	0.8710
8.7000	0.8913
8.8000	0.9119
8.9000	0.9327
9.0000	0.9539
9.1000	0.9753
9.2000	0.9970
9.3000	1.0189
9.4000	1.0411
9.5000	1.0635
9.6000	1.0861
9.7000	1.1088
9.8000	1.1318
9.9000	1.1549
10.0000	1.1782
10.2000	1.2252
10.4000	1.2727
10.6000	1.3208
10.8000	1.3693
11.0000	1.4181
11.2000	1.4673
11.4000	1.5168
11.6000	1.5668
11.8000	1.6168

x, in.	r, in.
12.0000	1.6670
12.2000	1.7173
12.4000	1.7679
12.6000	1.8186
12.8000	1.8694
13.0000	1.9205
13.2000	1.9716
13.4000	2.0229
13.6000	2.0743
13.8000	2.1258
14.0000	2.1774
14.2000	2.2290
14.4000	2.2807
14.6000	2.3324
14.8000	2.3842
15.0000	2.4360
15.2000	2.4877
15.4000	2.5394
15.6000	2.5912
15.8000	2.6431
16.0000	2.6950
16.2000	2.7469
16.4000	2.7988
16.6000	2.8506
16.8000	2.9022
17.0000	2.9535
17.2000	3.0046
17.4000	3.0554
17.6000	3.1060
17.8000	3.1563
18.0000	3.2063
18.2000	3.2561
18.4000	3.3056
18.6000	3.3548
18.8000	3.4037
19.0000	3.4522
19.2000	3.5006
19.4000	3.5486
19.6000	3.5963
19.8000	3.6437
20.0000	3.6909
20.3000	3.7610
20.6000	3.8305
20.9000	3.8993
21.2000	3.9675
21.5000	4.0350
21.8000	4.1019
22.1000	4.1682
22.4000	4.2338
22.7000	4.2988
23.0000	4.3631
23.3000	4.4269
23.6000	4.4900
23.9000	4.5526
24.2000	4.6144
24.5000	4.6757
24.8000	4.7365
25.1000	4.7966

Table 6. (continued)

x, in.	r, in.
25.4000	4.8561
25.7000	4.9152
26.0000	4.9735
26.3000	5.0314
26.6000	5.0886
26.9000	5.1453
27.2000	5.2015
27.4999	5.2572
27.7999	5.3123
28.0999	5.3668
28.3999	5.4208
28.6999	5.4743
28.8999	5.5097
29.1999	5.5623
29.4999	5.6145
29.7999	5.6661
29.9999	5.7002
30.4999	5.7846
30.9999	5.8677
31.4999	5.9494
31.9999	6.0298
32.4999	6.1091
32.9999	6.1870
33.4999	6.2637
33.9999	6.3393
34.4999	6.4136
34.9999	6.4868
35.4999	6.5588
35.9999	6.6297
36.4999	6.6994
36.9999	6.7679
37.4999	6.8354
37.9999	6.9017
38.4999	6.9670
38.9999	7.0313
39.5000	7.0945
40.0000	7.1567
40.5000	7.2178
41.0000	7.2780
41.5000	7.3372
42.0000	7.3954
42.5000	7.4527
43.0000	7.5091
43.5000	7.5645
44.0000	7.6190
44.5000	7.6726
45.0000	7.7253
45.5000	7.7772
46.0000	7.8282
46.5004	7.8783
47.0004	7.9276
47.5004	7.9761

x, in.	r, in.
48.0004	8.0237
48.5004	8.0705
49.0004	8.1166
49.5004	8.1619
50.0004	8.2064
51.0004	8.2931
52.0004	8.3769
53.0004	8.4577
54.0004	8.5358
55.0004	8.6110
56.0008	8.6836
57.0008	8.7535
58.0008	8.8210
59.0008	8.8860
60.0008	8.9485
61.0008	9.0087
62.0008	9.0665
63.0008	9.1222
64.0012	9.1756
65.0012	9.2267
66.0012	9.2758
67.0012	9.3227
68.0012	9.3678
69.0012	9.4108
70.0012	9.4519
71.0012	9.4912
72.0012	9.5287
73.0016	9.5643
74.0016	9.5983
75.0016	9.6306
76.0016	9.6612
77.0016	9.6903
78.0016	9.7177
79.0016	9.7437
80.0016	9.7682
81.0016	9.7913
82.0016	9.8130
83.0020	9.8334
84.0020	9.8524
85.0020	9.8701
86.0020	9.8867
87.0020	9.9019
88.0020	9.9157
89.0020	9.9283
90.0020	9.9396
91.0024	9.9501
92.0024	9.9597
93.0024	9.9685
94.0024	9.9767
95.0024	9.9845
95.5024	9.9882
95.7024	9.9897

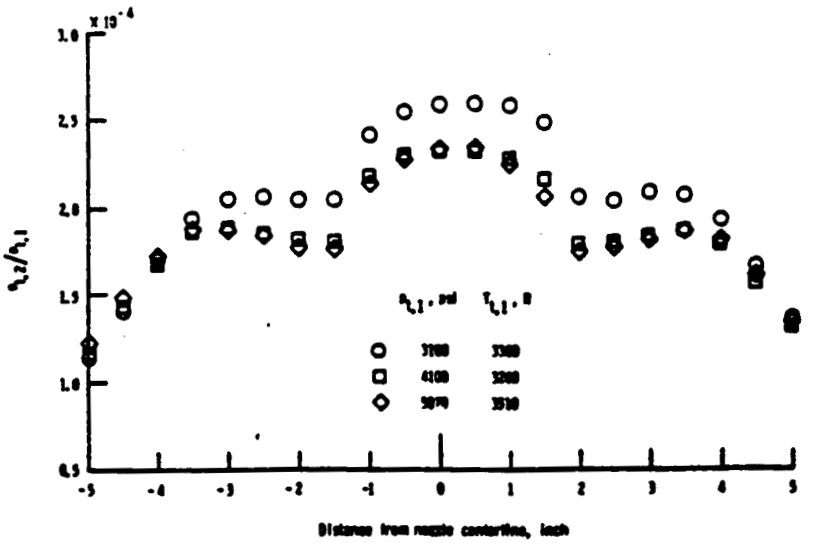

Fig. 1.1 Pitot-pressure profiles in test section of Nitrogen Tunnel.

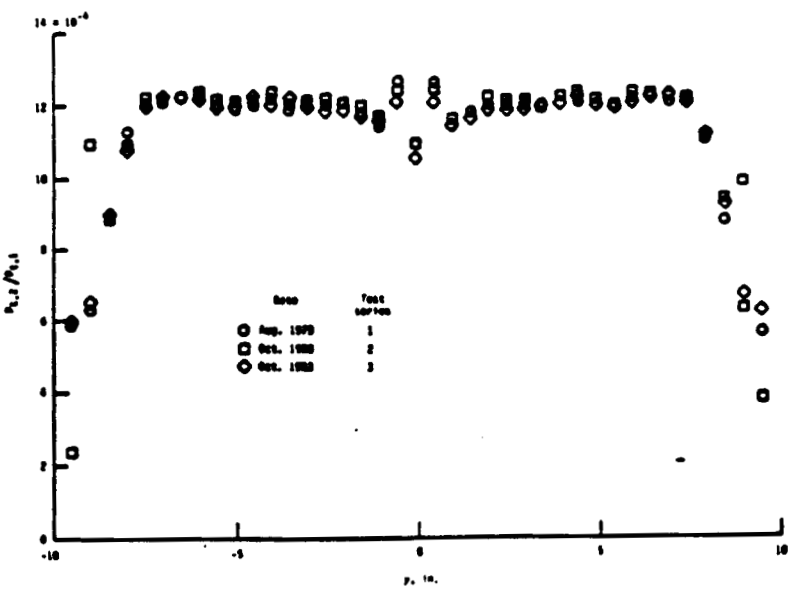

Fig. 1.2 Pitot-pressure profiles in test section of CF_4 Tunnel.

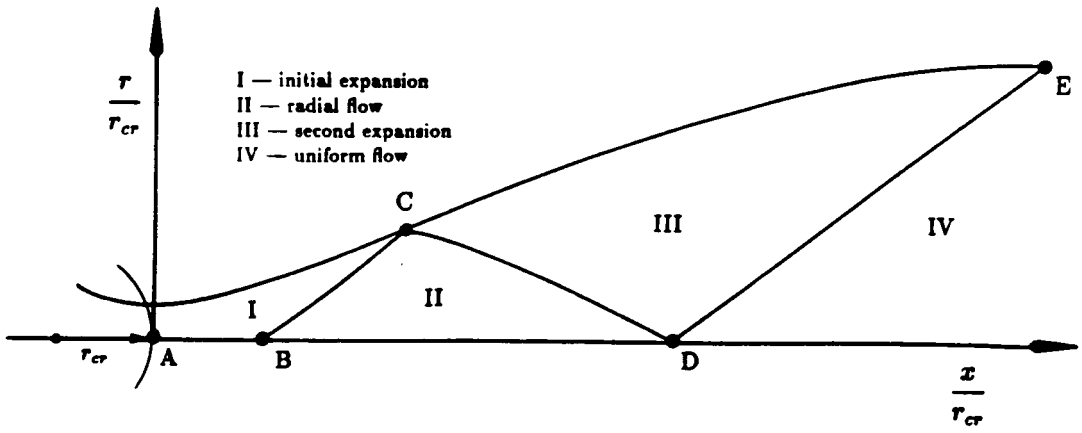

Fig. 1.3 Contoured nozzle schematic for design MOC.

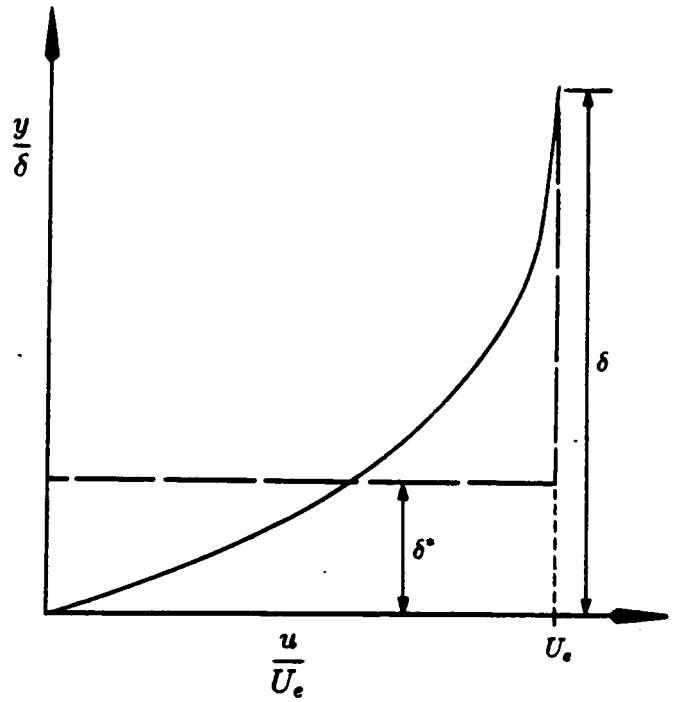

Fig. 1.4 Schematic of displacement thickness.

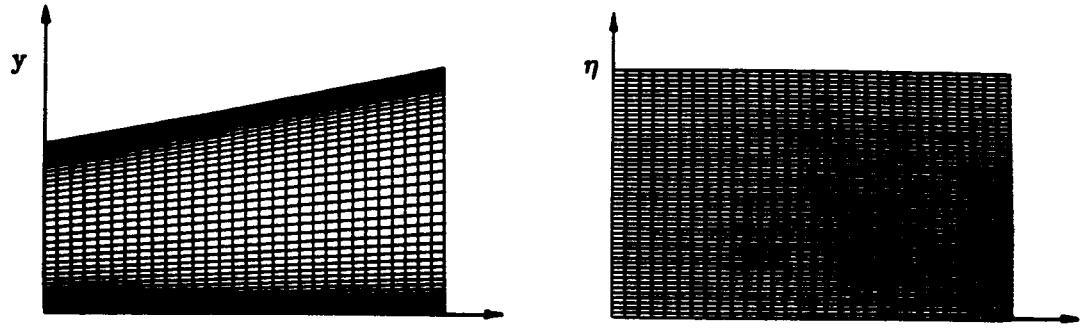

a) physical domain

b) computational domain

Fig. 3.0 Grid transformation.

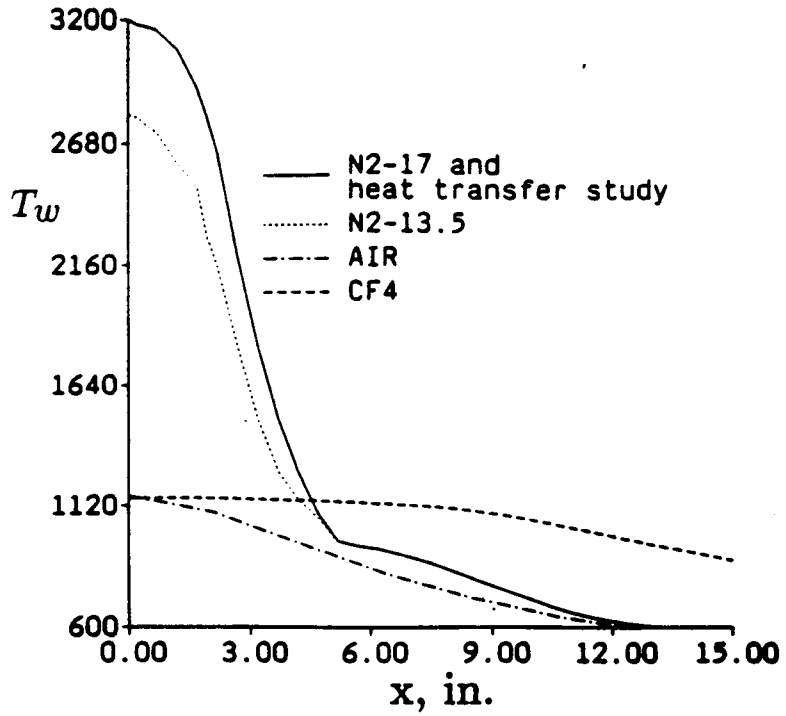

Fig. 6.0 Design wall temperature distributions.

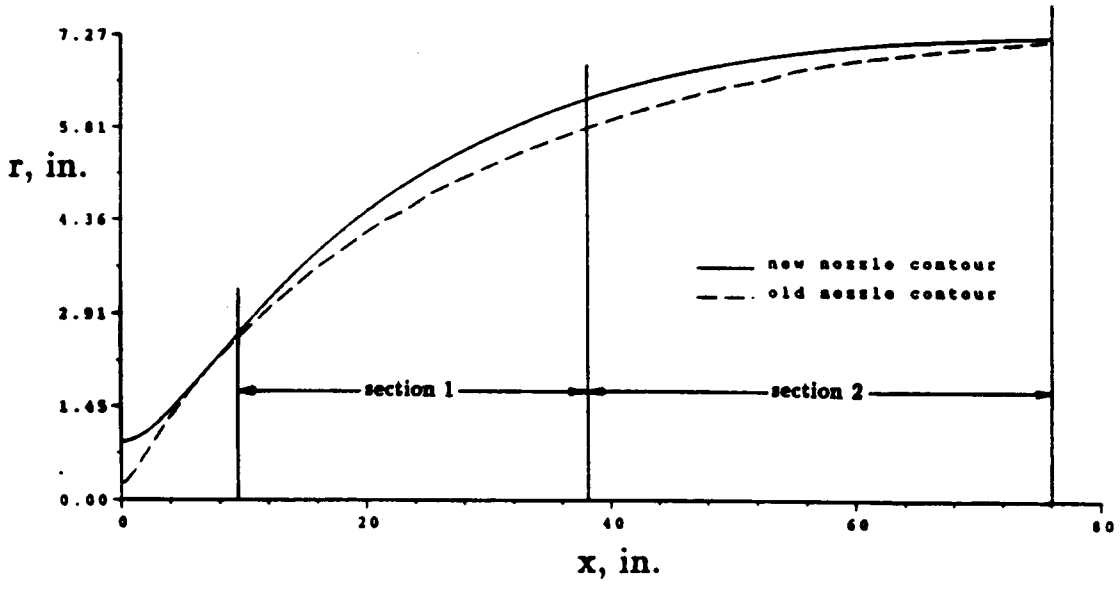

Fig. 6.1.1 Air nozzle contour compared to existing Mach 10 nozzle.

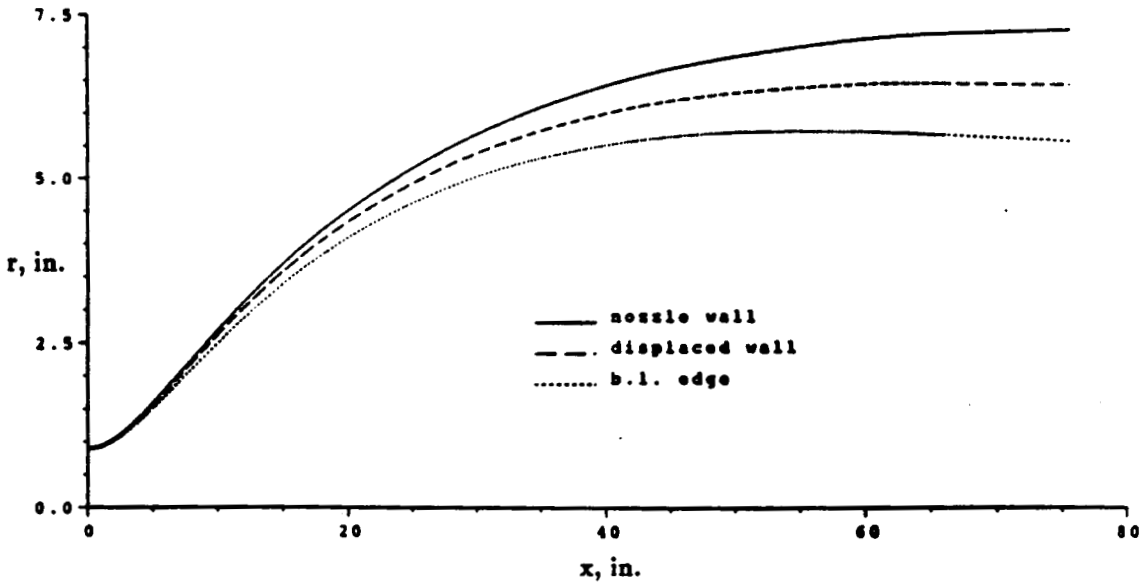

Fig. 6.1.2 Air nozzle contour including boundary layer and displacement thickness.

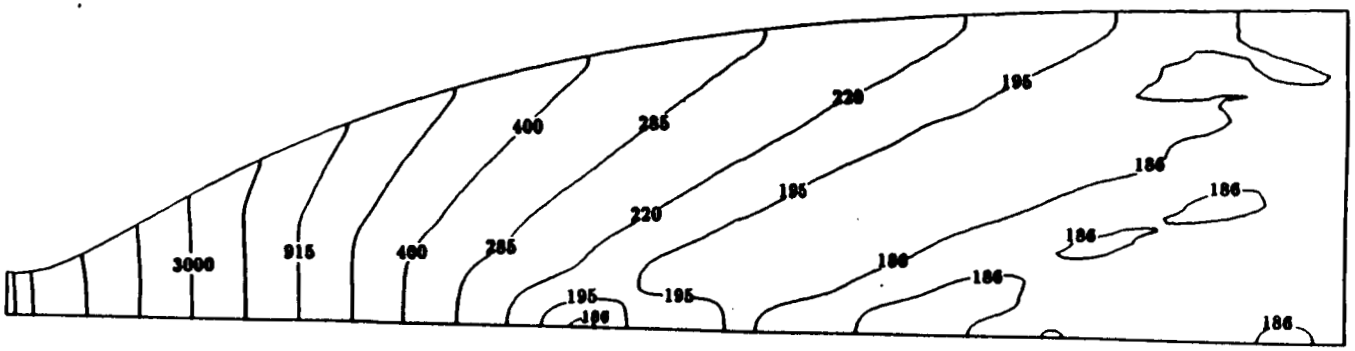

Fig. 6.1.3 Navier-Stokes static pressure contours in Air nozzle.

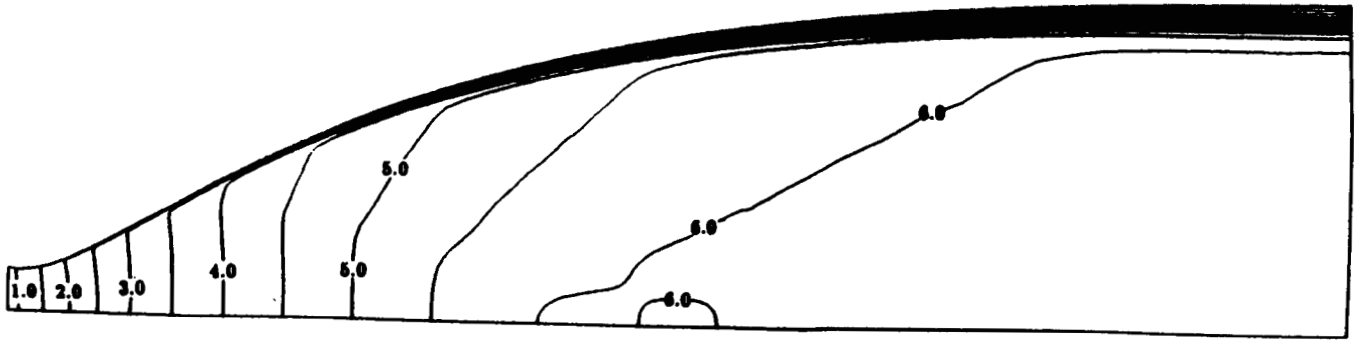

Fig. 6.1.4 Navier-Stokes Mach number profiles in Air nozzle.

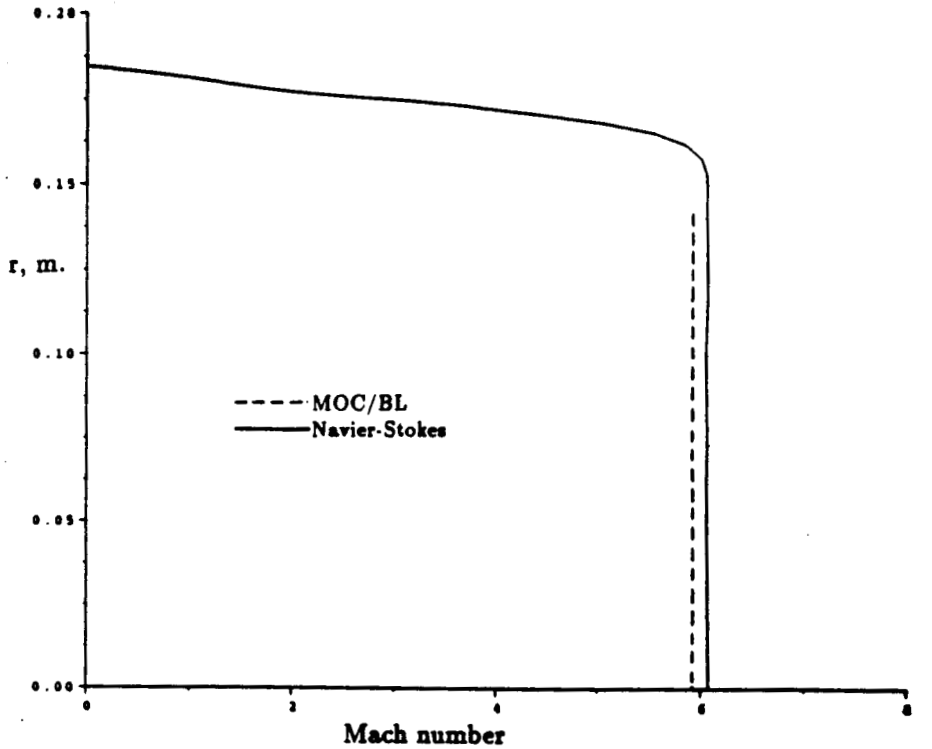

Fig. 6.1.5 Exit plane Mach number profile for Air nozzle.

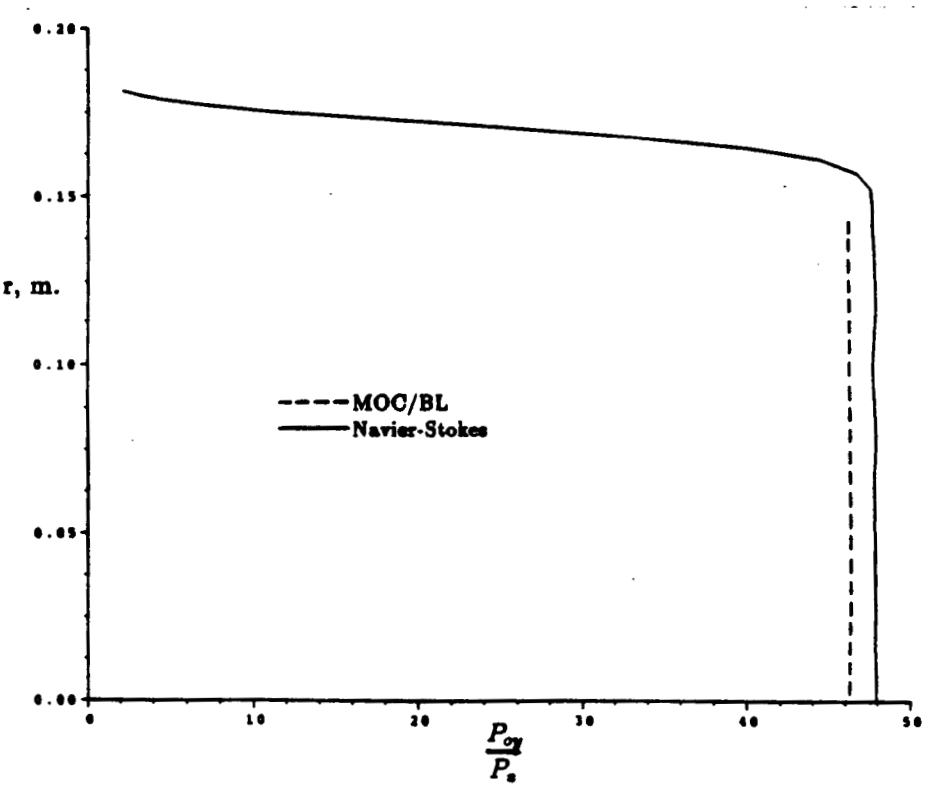

Fig. 6.1.7 Pressure ratio across normal shock wave for Air nozzle.

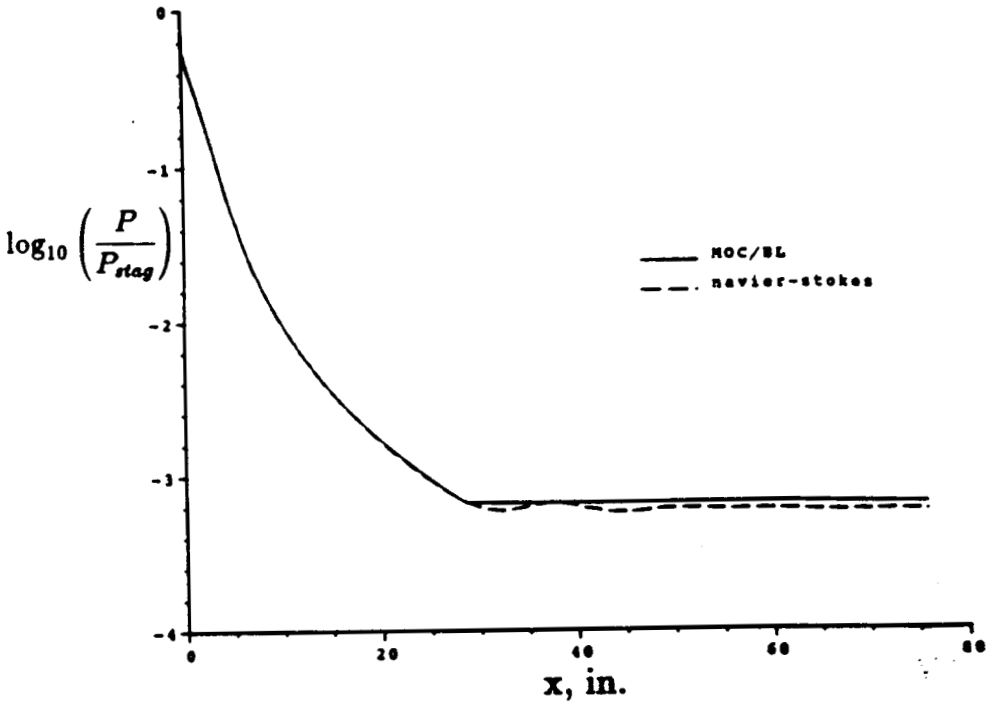

Fig. 6.1.6 Centerline pressure ratio for Air nozzle.

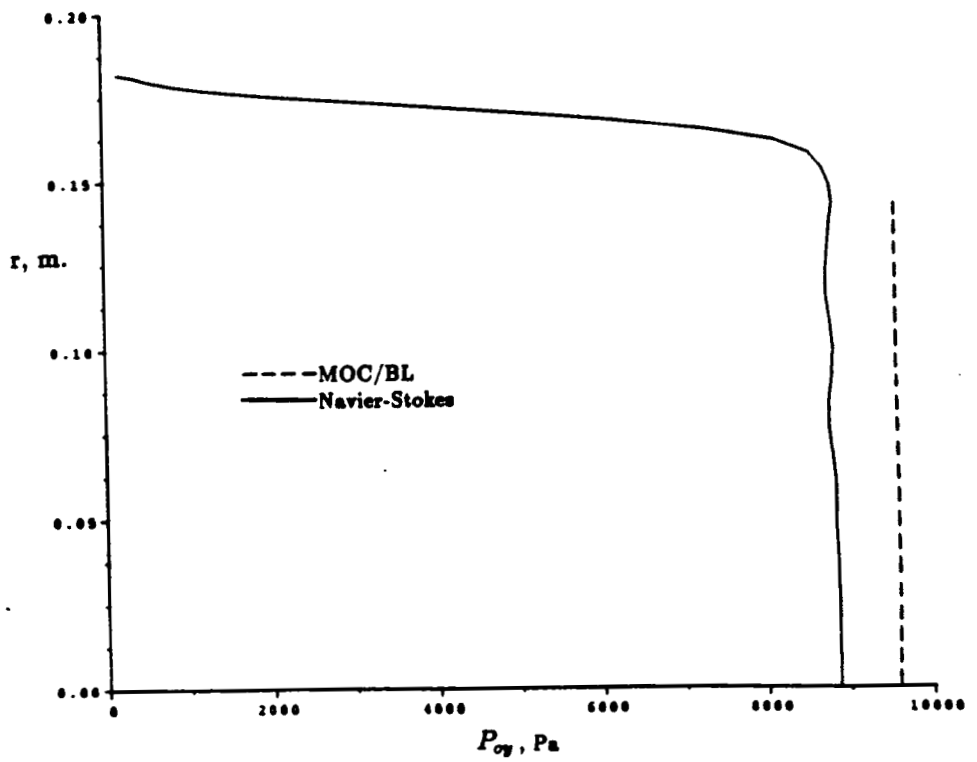

Fig. 6.1.8 Total pressure profile downstream of normal shock in exit plane of Air nozzle.

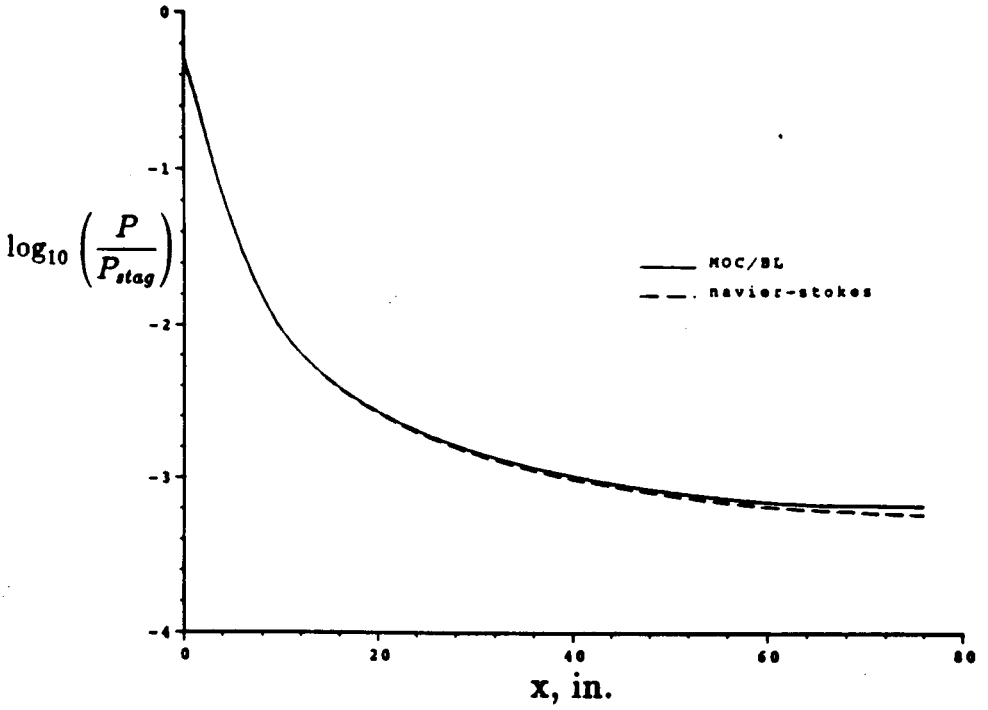

Fig. 6.1.9 Wall pressure ratio for Air nozzle.

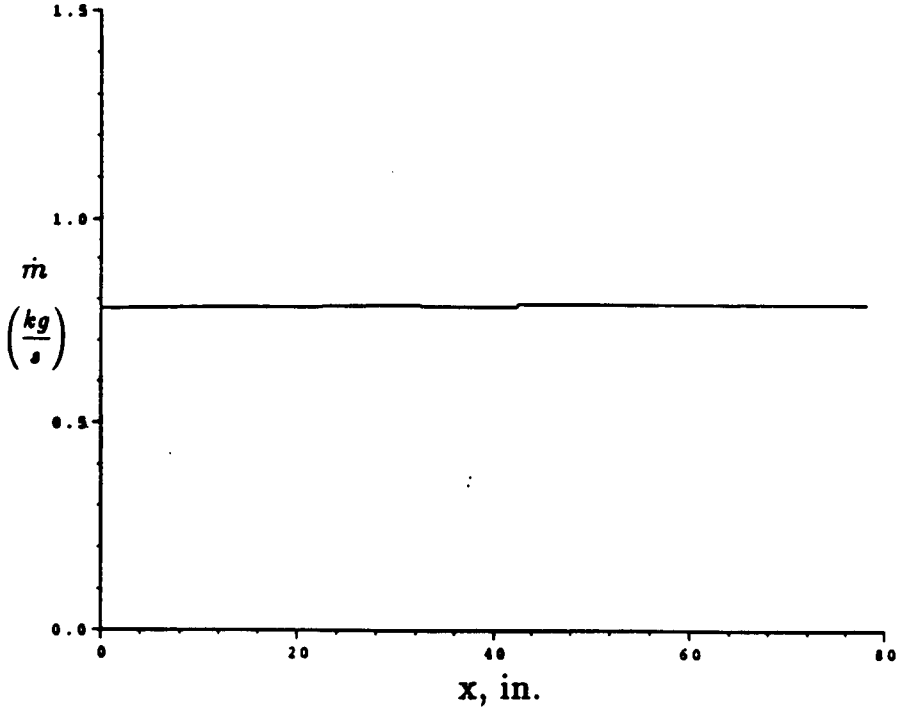

Fig. 6.1.10 Navier-Stokes massflow rate for Air nozzle.

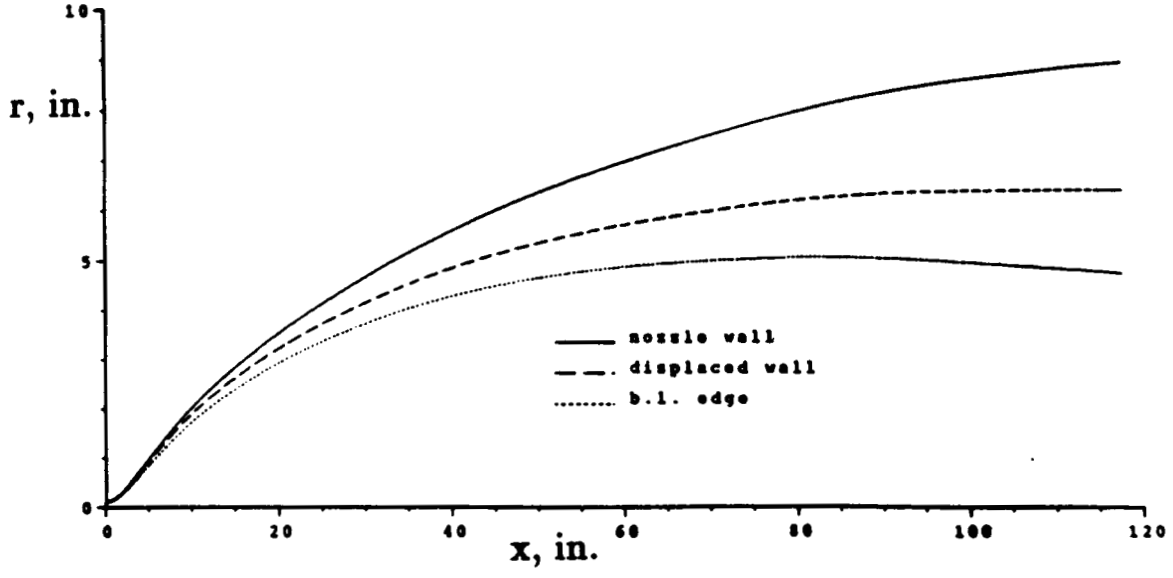

Fig. 6.2.1 $N_2 - 13$ nozzle contour including boundary layer and displacement thickness.

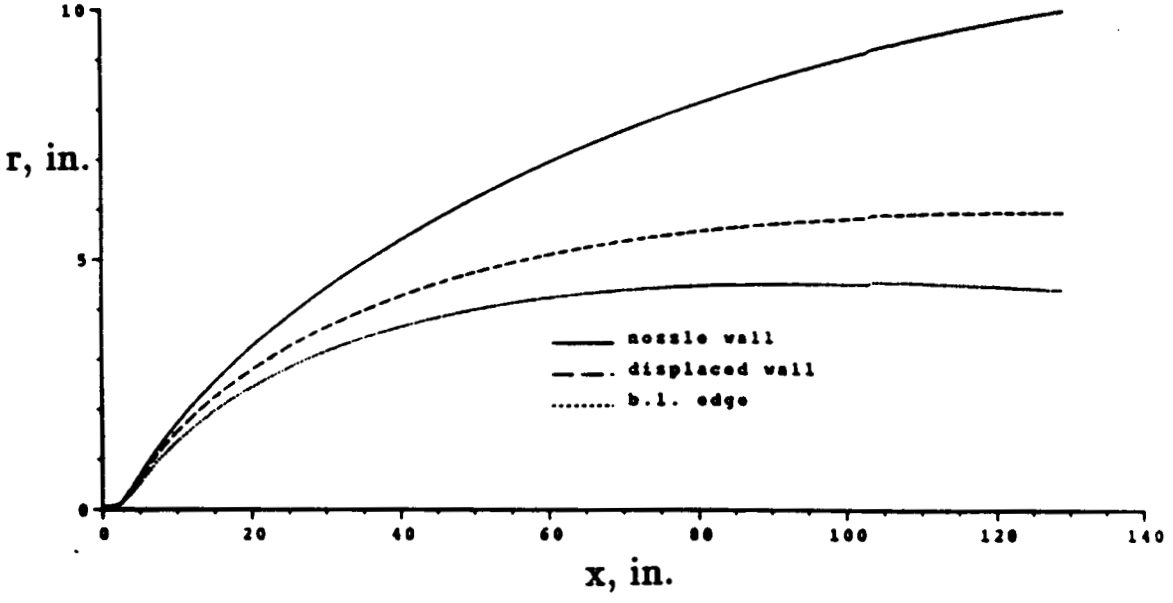

Fig. 6.2.2 $N_2 - 17$ nozzle contour including boundary layer and displacement thickness.

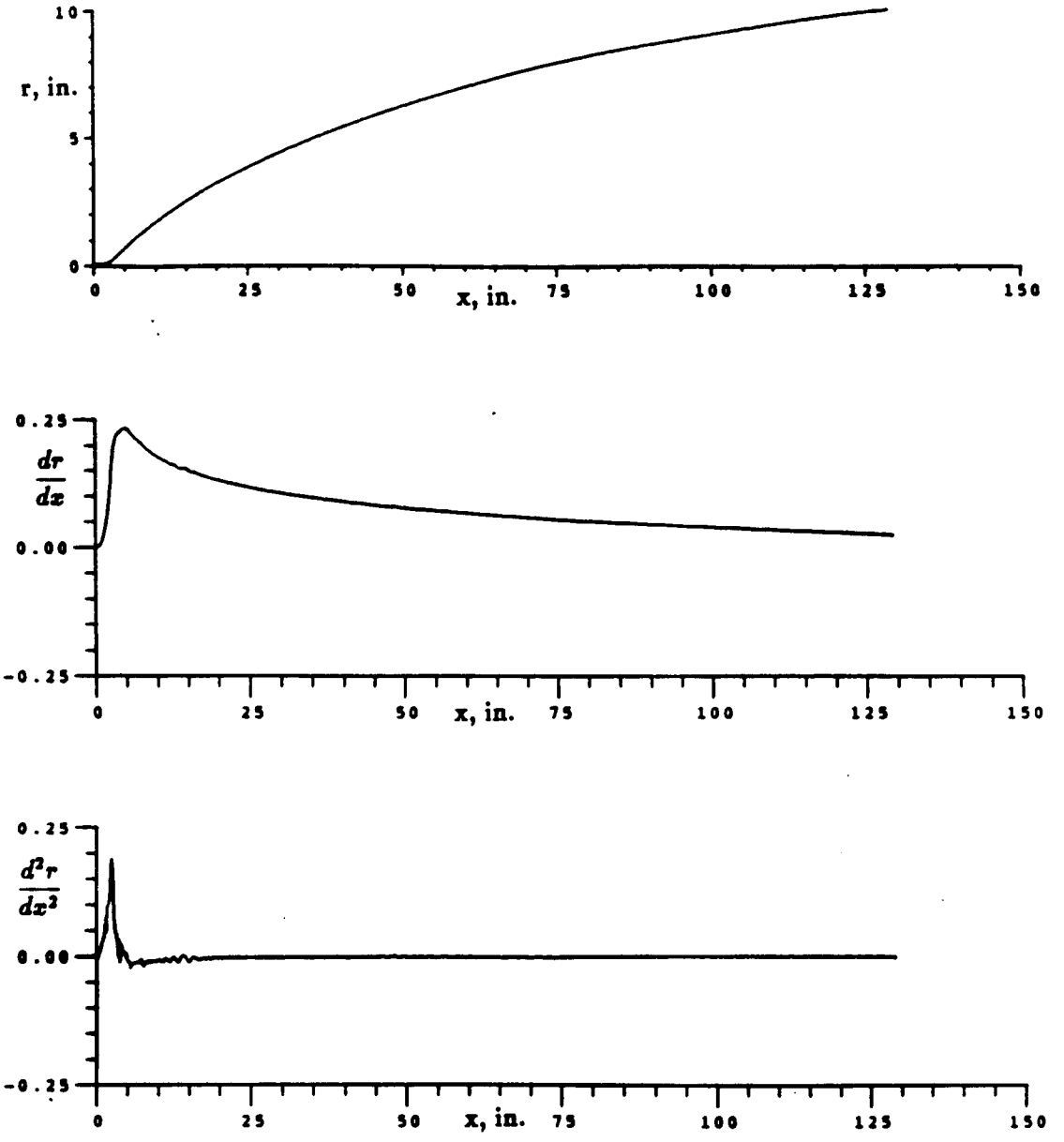

Fig. 6.2.3 Smoothed $N_2 - 17$ contour, slope and curvature.

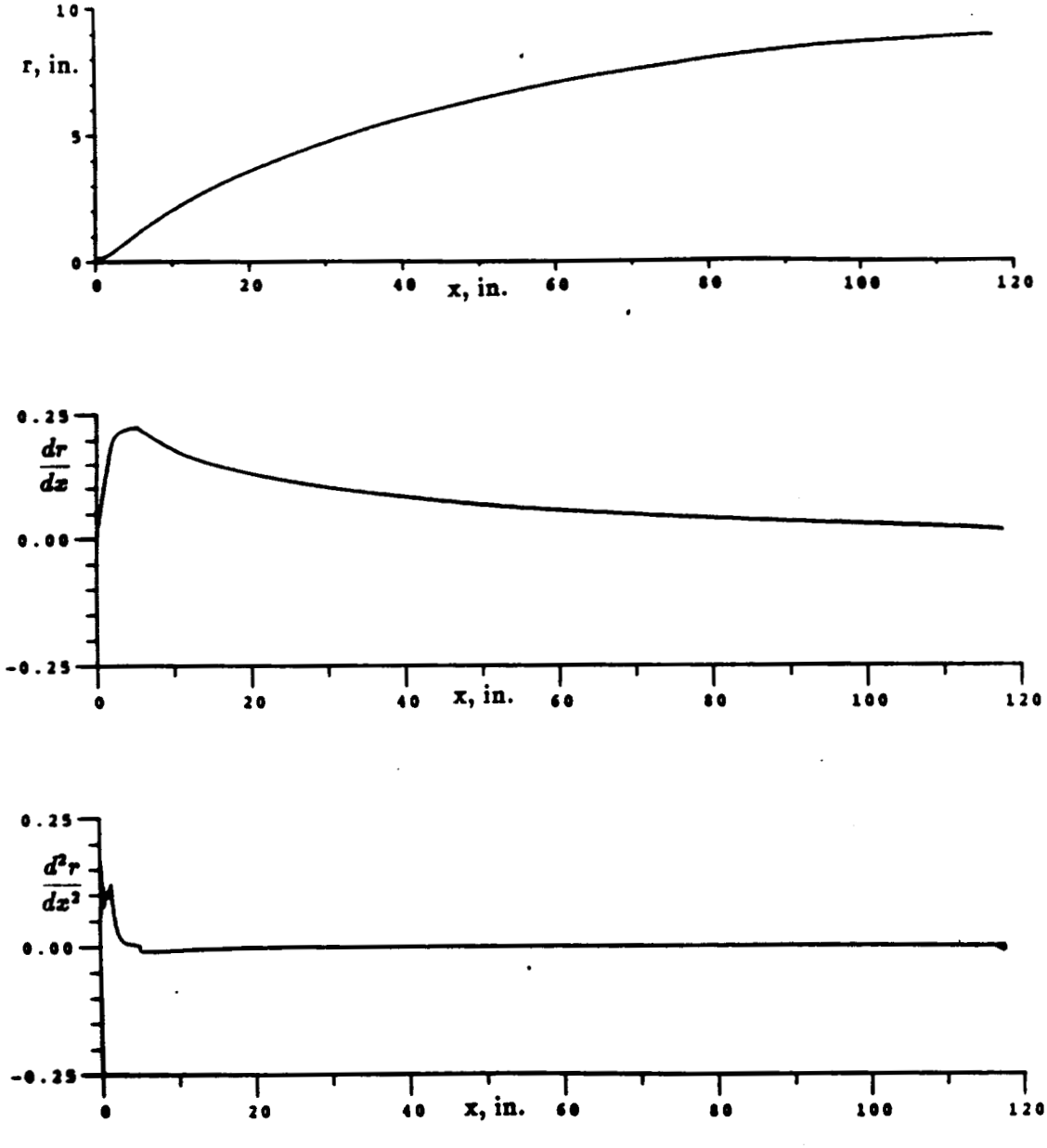

Fig. 6.2.4 $N_2 - 13$ contour, slope and curvature.

C-2

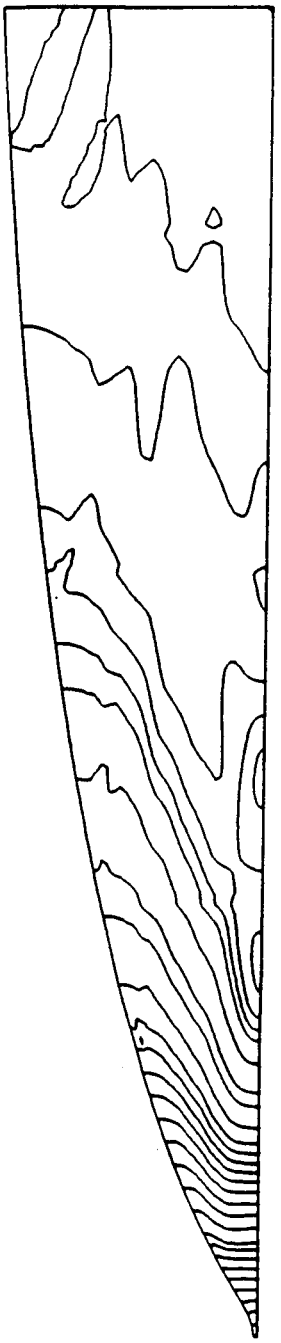

Fig. 6.2.5 Navier-Stokes static pressure contours for $N_2 - 13$ nozzle.

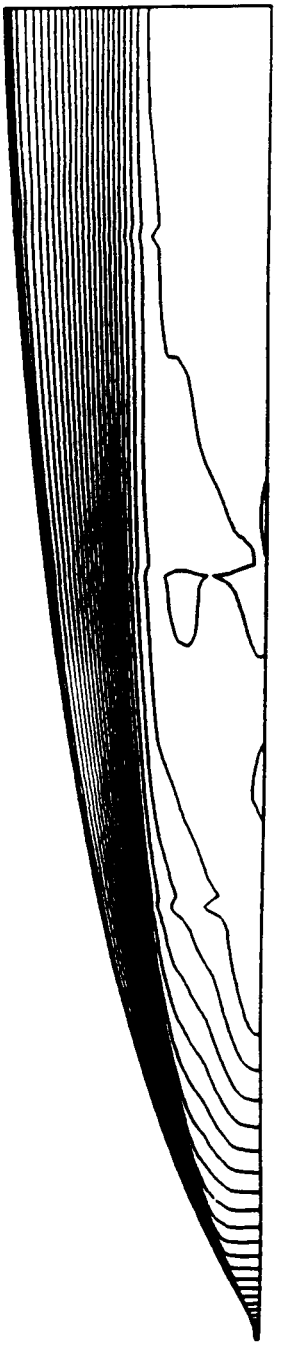

Fig. 6.2.6 Navier-Stokes Mach number contours for $N_2 - 13$ nozzle.

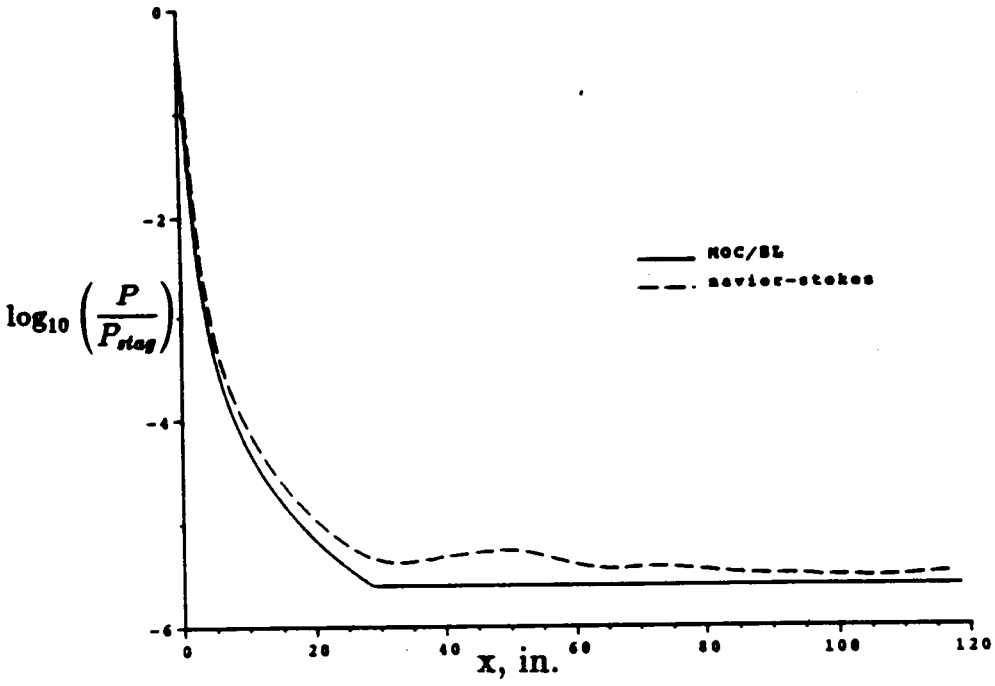

Fig. 6.2.7 Centerline pressure ratio for $N_2 - 13$ nozzle.

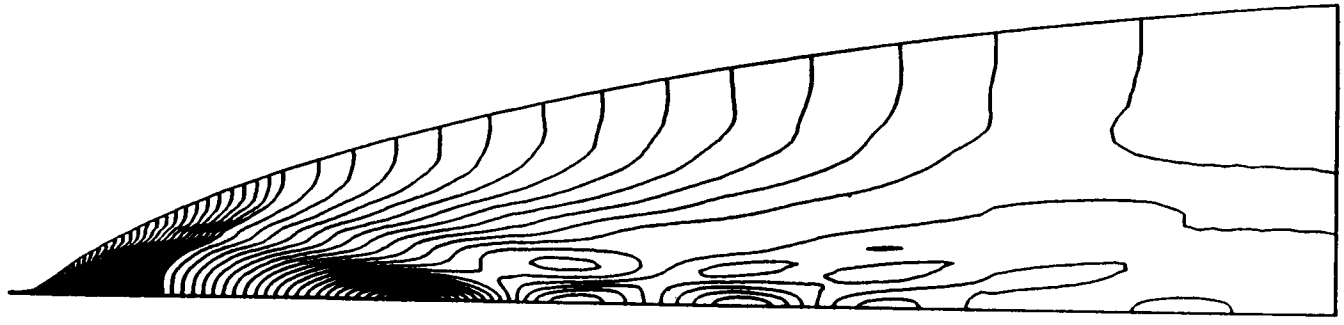

Fig. 6.2.8 Navier-Stokes static pressure contours for $N_2 - 17$ nozzle.

Fig. 6.2.9 Navier-Stokes Mach number contours for $N_2 - 17$ nozzle.

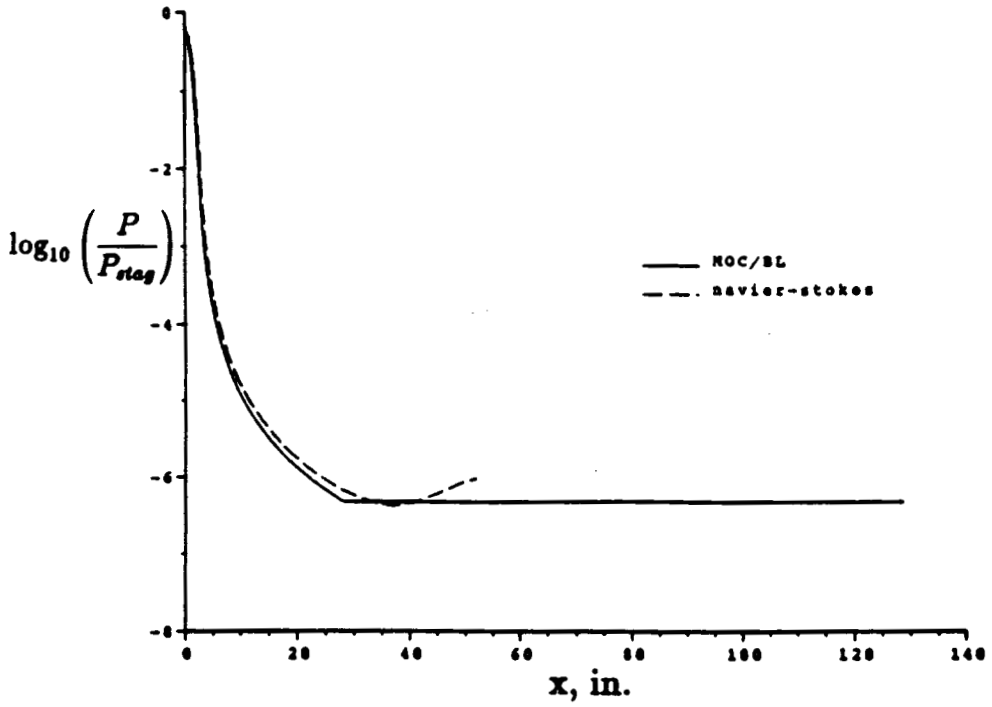

Fig. 6.2.10 Centerline pressure ratio for $N_2 - 17$ nozzle (first wall temp.).

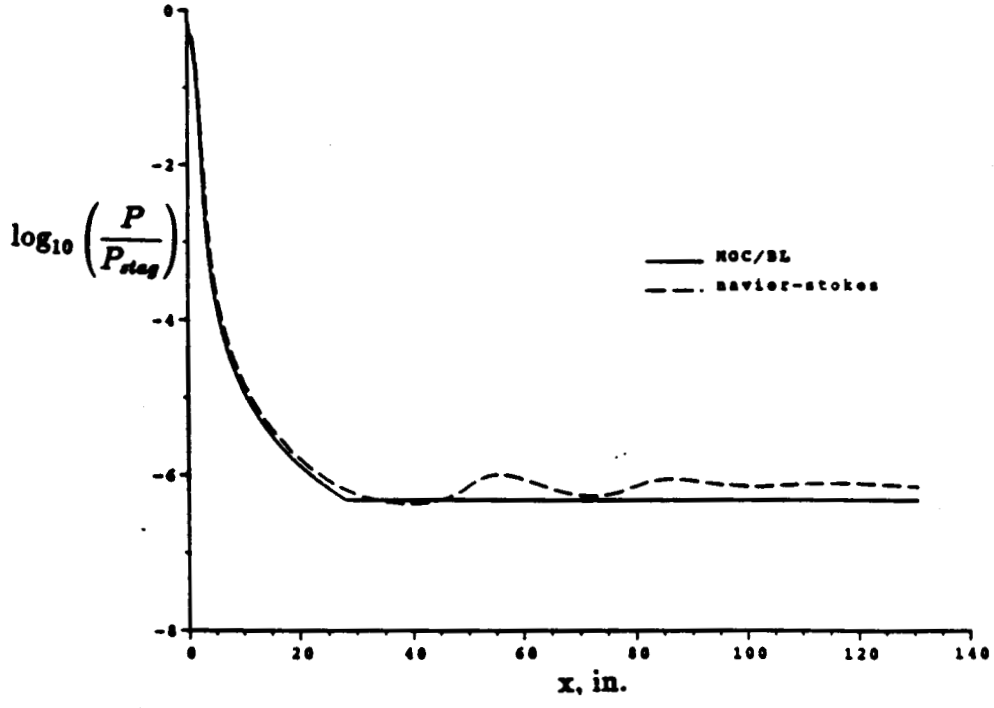

Fig. 6.2.11 Centerline pressure ratio for $N_2 - 17$ nozzle (Kumar).

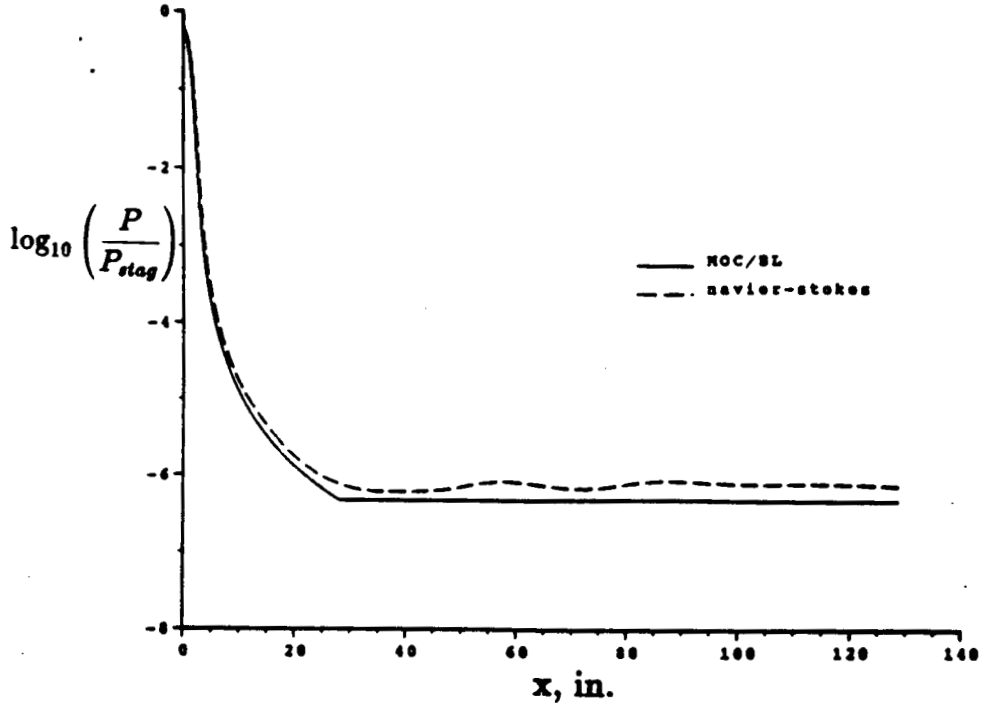

Fig. 6.2.12 Centerline pressure ratio for $N_2 - 17$ nozzle (second wall temp.).

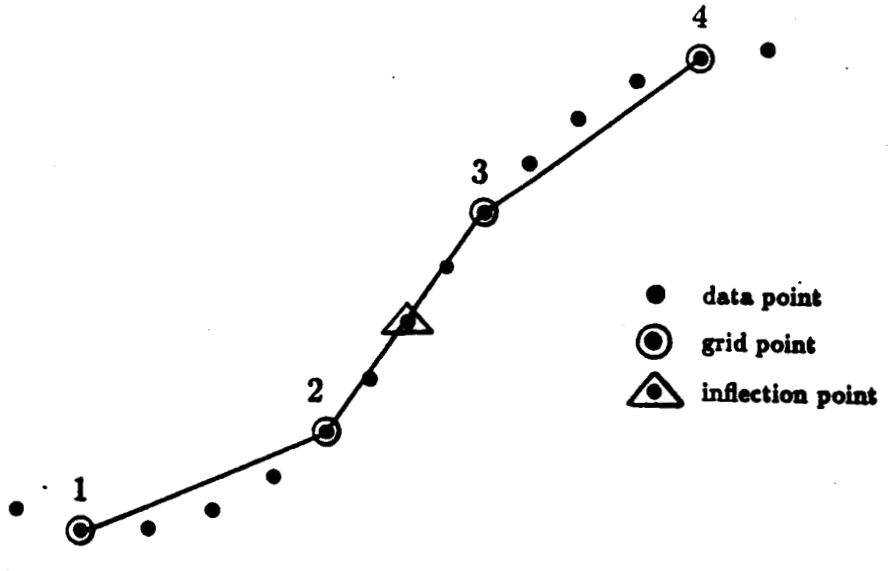

Fig. 6.2.13 Movement of inflection point due to discretization.

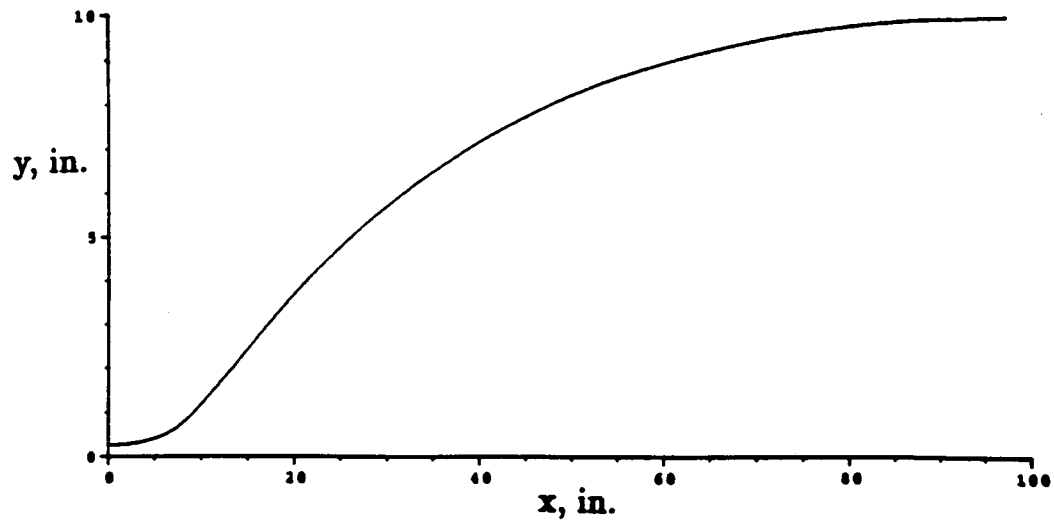

Fig. 6.3.1 CF_4 **nozzle contour.**

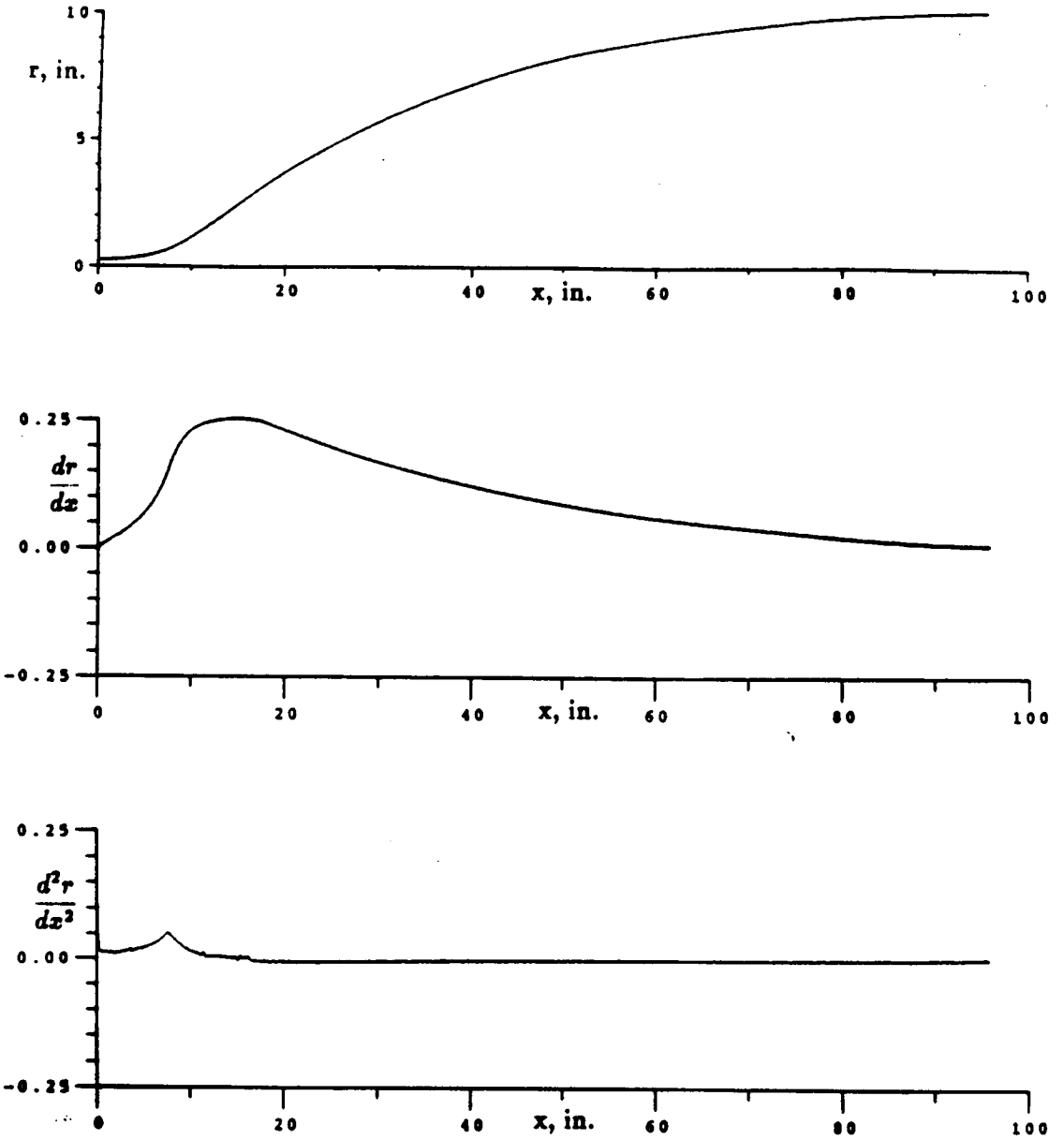

Fig. 6.3.2 Smoothed CF_4 contour, slope and curvature.